Natural extract-polymer monodisperse submicron particles from Plateau-Rayleigh microjets

Elena Barbero-Colmenar [a], Eszter Bodnár [a], Joan Rosell-Llompart [a,b,*]

[a] Department of Chemical Engineering, Universitat Rovira i Virgili, E-43007, Tarragona, Spain

[b] Catalan Institution for Research and Advanced Studies - ICREA, E-08010, Barcelona, Spain

Abstract

Particles of interest in food, pharmaceutical, and nutraceutical sectors are often formulated with a polymer and one or more natural or synthetic active compound. The two components frequently have distinct hydrophilicity. Submicrometric particles with narrow size dispersion can be made by the droplet-to-particle route by electrospray. In the steady cone-jet mode a liquid Taylor cone (TC) continuously emits a Plateau-Rayleigh microjet which breaks up spontaneously and periodically into tiny droplets, which later dry up to form solid particles. To achieve a stable process of this kind, we argue that it is necessary to: (i) operate near the minimum solution flow rate compatible with TC stability, (ii) prevent the drying of the TC by surrounding it with a gentle gas stream saturated in solvent vapor, and (iii) monitor the electric current and image the TC. We demonstrate this process in the preparation of curcumin (CUR) loaded polyvinylpyrrolidone (PVP) submicrometric particles as a function of solution composition and ambient relative humidity. In the atomization step (jet and droplet formation), the initial droplet size and charge are determined by the liquid properties and flow rate. The particles' shapes were spherical (with or without internal voids), corrugated due to shell buckling (with compact interiors), and filamented due to Coulombic instabilities, depending on the interplay of different factors at the droplet drying step. These included the droplet size and charge, solvent evaporation, solute diffusion, water uptake from the ambient, mechanical forces, and solution thermodynamics. The electric current and droplet size are suitably predicted by scaling laws developed for simple Newtonian fluids. Hence, our particle sizes lie always between the predicted droplet and compact-sphere sizes, at a distance which depends on the particle morphology. CUR-loaded PVP quasi-monodisperse submicron particles could be an interesting model for drug delivery and biomedical applications.

Keywords: Electrohydrodynamic atomization, Taylor cone, Plateau-Rayleigh, shell buckling, Polymer nanoparticles, FIB

1. Introduction

Droplet-to-particle conversion offers a versatile and efficient manufacturing route for powder production, applicable to diverse materials, particle sizes and morphologies [1]. The particles often consist of polymers and natural or synthetic additives which have distinct hydrophilicity, bringing richness to the particle formation mechanisms, and thus to the particle morphologies. Industrially, Spray Drying is the most widely used droplet-to-particle approach, being suitable for preparing food, pharmaceutical, and nutraceutical particles [2–5]. Yet, an unmet challenge of Spray Drying is achieving narrow dispersion of the particle size (e.g., GSD <1.2) in the submicron range (<1 μm in diameter) [4,6–8].

The key to obtaining small uniform particles by the droplet-to-particle route lies in making small and uniformly sized droplets in the liquid atomization step. Electrospray (ES), also known as electrohydrodynamic atomization or EHDA, is a liquid atomization method uniquely capable of producing very fine droplets with very narrow size dispersion [9–11] unlike more conventional hydrodynamic, pneumatic and ultrasonic liquid atomization methods typically employed in Spray Drying [12–15]. In addition, ES is free of nozzle clogging problems, unlike jet atomization technologies using micron-sized apertures. At the same time, it enjoys exquisite control over the particle morphology through the solvent(s) in the precursor solutions, the solute concentration, and the ambient conditions [16,17]. This is important because the function of the electrosprayed particles depends on their morphology in materials applications like drug delivery [18–22], energy [23,24] and food applications [25,26].

Electrospray is based on the electrification of the precursor liquid, which is usually flowing out of a capillary tube at a given rate. At the appropriate flow rate and electrical potential, a conical meniscus called Taylor cone (TC) is established, whose tip ejects a microscopic liquid jet which breaks up spontaneously and periodically by the Plateau-Rayleigh instability into nearly identical droplets [9,16,27]. The conversion of electrical energy to droplet surface energy is highly efficient. In addition, the method is up-scalable through the multiplexing of emission points [28–35]. Recently, a modification of the electrospray process was proposed [36,37] based on the discharging of the

electrospray droplets, expanding the possibilities for scaling up when seeking monodisperse particles. Electrospray also allows the formation of particles with different architectures, such as core-shell particles and multi-layered particles also known as Yolk-shell particles [38–41]. In sum, electrospray is a simple-to-use and powerful way to produce submicron particles with material and morphology versatility, as claimed in various reviews [14,18,19,42–45].

Even so, as a particle engineering tool, ES requires careful selection of the operating parameters. This is especially true when atomizing complex solutions, such as those containing polymeric components, additives and volatile solvents. (i) First, it is critical to identify the spraying mode, and to avoid dripping modes, which are triggered by inadequate (often excessive) liquid flow rates [46,47]. The smallest and most monodisperse droplets can be obtained by operating in the Steady Cone-Jet (SCJ) mode, in which the jet emission from the TC does not fluctuate and is sustained within a flow rate window which depends on the liquid properties. (ii) Second, the most monodisperse droplets are obtained by avoiding jet whipping (an instability caused by excessive electrification), which can be achieved by choosing the flow rate to be close to the minimum allowed value Q_{min} [11,27,48,49]. (iii) Third, the SCJ mode uses low flow rates, solvent evaporation from the TC can cause any non-volatile solutes to precipitate at the TC, eventually destabilizing it [16]. This issue can be effectively solved by surrounding the TC with a gentle solvent-saturated gaseous flow (as we shall prove). Despite their usefulness for particle production by ES, however, such sheath coflows have not been used except by a handful of research groups [16,50,51]. Instead, high flow rates ($Q \gg Q_{min}$) are often favored in the literature to increase overall particle production and to get stable spraying. Unfortunately, high flow rates result in bigger droplets (typically tens of microns and larger) and in the broadening of the droplets' size distribution. (iv) Lastly, besides flow rate, an important control parameter is relative humidity as ambient moisture can be absorbed by the drying droplets, and act as a non-solvent or as a non-soluble template [16,52].

In this work, we show how these principles apply to the electrospraying of polymeric solutions for making submicron particles of a poorly water-soluble drug encapsulated in a hydrophilic polymer. Such chemical combinations are of interest for pharmaceutical particles in the form of amorphous solid

dispersion (ASDs) [12,53–55]. We have chosen polyvinylpyrrolidone (PVP) as the encapsulating polymer and curcumin (CUR) as the model drug. PVP is widely used in ASDs, often in combination with poorly soluble drugs to improve their aqueous solubility [56–60]. PVP has been used as a drug carrier for oral [61–63], transdermal [64,65], inhalable [66,67], and ocular administrations [68]. CUR, a natural extract, is well-known for its anti-inflammatory, antioxidant, and anti-cancer properties [69–72]. Improved CUR aqueous solubility and bioavailability have been achieved with PVP-based nano-formulations made by supercritical assisted atomization [73], spray drying [74,75] and even electrospray [76,77]. However, a systematic study connecting particle morphology to the electrospray process conditions, and the droplet and particle formation mechanisms, requires a precisely controlled liquid atomization process.

We specifically investigate the conditions for ES formation of amorphous CUR-PVP particles in the SCJ mode over a wide range of polymer and drug concentrations in volatile solvents, with the goal to demonstrate stable operation at as high solute concentrations as possible, and to identify the conditions which lead to globular size-monodisperse submicron particles. Theoretical predictions from established cone-jet physics models for simple fluids exist for the minimum flow rate, the electrical current, and the droplet size [27,47,78]. Therefore, we assess such predictions in our system and use the theoretical droplet size to help us interpret the particle size and morphology data. These models previously compared favorably with the sizes of compact particles by Hogan et al. [79]. However, in that study, the Taylor cone was not protected from drying. To relate the particle size to the droplet size it is critical to know that the solution composition does not change in the cone-jet due to solvent evaporation. Here, we prevent solvent evaporation from the TC by the mentioned solvent-saturated gas coflow. This flow is kept much lower than the gas chamber flow, to have an influence on the cone-jet but not the spray, allowing to impose an independent composition in the chamber gas. In this way, we are able to introduce water vapor into the chamber to study the effect of water on the droplet-to-particle formation, without altering the droplet formation. Previously, we observed pronounced effects on the particle morphology due to water vapor in the case of water insoluble polymers [16] . Here, we

expand our scope with a hydrophilic polymer (PVP) with the addition of a hydrophobic compound (CUR).

First, we identify the polymer concentration window in a suitable solvent (ethanol) which forms size-monodisperse particles, and then, we address the challenge of dissolving large amounts of the model drug (high drug-polymer ratio), while still obtaining size-monodisperse globular particles in amorphous state. To achieve high solubilities, we show ethanol/acetone (1:1 v/v) to be suitable. For both solvent systems studied, we have systematically varied both the process parameters (significantly, low solution flow rates) and the properties of the specific solution (significantly, its electrical conductivity). In all conditions, we interpret the various morphologies of the particles collected after droplet drying. We also show the importance of controlling the ambient relative humidity, and we report its effects on the particle morphology. Particle size and morphology are characterized by scanning electron microscopy (SEM) combined with a focused ion beam (FIB) to evaluate internal particle structure, while the chemical structure and crystallinity of the prepared particles are evaluated using Fourier-transform infrared spectroscopy (FTIR) and X-ray diffraction (XRD), respectively.

2. Materials and methods

2.1. Materials and solutions characterization

The chemical reagents were used as purchased, without further purification. Curcumin (CUR 99% purity, CAS Number 458-37-7, 368.38 g/mol) and polyvinylpyrrolidone (PVP, CAS Number 9003-39-8, weight-average molecular weight (Mw) 40 kDa) were purchased from Sigma Aldrich. Ethanol absolute (min. 99.9% purity, ACS reagent grade, CAS Number 64-17-5) and acetone (min. 99.8% purity, ACS reagent grade, CAS Number 67-64-1) were purchased from Scharlau. Dry nitrogen (Carburos Metálicos, Premier grade) was used as a gas carrier.

Solutions with different CUR-PVP weight ratios were prepared by adding PVP and CUR to the solvent system -either ethanol or ethanol/acetone (1:1 v/v)- at room temperature, and then magnetically stirring until complete dissolution. The solution compositions and main properties which influence the TC formation, and the jet breakup processes are shown in Table 1. Electrical

conductivities were determined with a portable conductivity meter (CRISON 35) using a glass-body probe (CRISON 50 61). The uncertainty on the conductivity values is ±5%, according to the quality-control certification of the probe. Kinematic viscosity measurements were made with a Cannon-Fenske viscometer (size 50), and density using a 5 mL Gay-Lussac pycnometer. The uncertainty of the individual density determinations is ±0.2%. All measurements were performed in triplicate and at room temperature (22.5 ± 3.0 °C) unless otherwise noted. Density was estimated for some compositions (details in Supplementary File, section SI.1). Due to the temperature uncertainty of ±3 °C, the overall uncertainty in the measured density values is ±0.5% (computed as the sum of the individual density determination and the impact of the temperature uncertainty on the densities of ethanol and acetone). Kinematic viscosity was measured only for specific solutions 5C-0P, 0C-5P and 5C-5P, whose dynamic viscosities (the product of kinematic viscosity and density) were 0.67, 1.45 and 1.61 mPa s, respectively. Over the studied concentration range, CUR did not significantly influence the solution density and viscosity, whereas both increased by the addition of PVP. The solution conductivity also increased with PVP concentration, while the addition of CUR for a fixed polymer concentration resulted in decreasing conductivity.

2.2. Electrospray setup and process

The experimental setup is shown in Fig. 1. It consists of a glass chamber (four parallel glass walls 175 x 130 x 1.8 mm) resting on an aluminum collector plate, and topped with a Delrin® plate which holds the needle assembly. Two glass panes rest on the collector plate onto two C-shaped spacers (not shown). These spacers define two slits between the aluminum plate and the other two glass panes. Through these slits, substrates for particle collection can be easily introduced in and out of the chamber while electrospraying. Either dry or humidified nitrogen is supplied into the chamber at a constant speed (ranged between 2.7 - 3.8 Lpm), exiting through the two slits. Relative humidity (RH) inside the chamber is monitored using a Vaisala HM34 probe inserted through a hole in the collector plate. RH was virtually zero (measured and reported as <5%) when only dry nitrogen was fed through the chamber. Humidified nitrogen was obtained by passing dry nitrogen through a bubbler containing deionized water. A Harvard Apparatus PHD 2000 syringe pump supplied polymeric

solution from a Hamilton glass syringe (500 or 1000 µL), at 0.75-1.5 µL/min through a Teflon© capillary tube (1/16 in OD, 300 µm ID) to the electrospraying needle (ES needle). The nominal accuracy of the infused flow rate is 0.35%. The needle is part of an assembly which comprises the ES needle (a square-ended metal capillary with 400/160 µm OD/ID) and a glass tube (2.00/1.16 mm OD/ID; length: 35 mm) which surrounds the needle and protrudes 0.3 mm from it. The purpose of the glass tube is to surround the needle tip with a 250 mm^3/s coflow gas stream saturated with solvent vapor of either ethanol (when electrospraying ethanolic solutions) or acetone (when electrospraying ethanol/acetone solutions). This methodology was previously used by Larsen et al. [50] and by us [16,51], and is very effective in preventing premature drying of the solution at the tip of the ES needle. As the gas is slightly undersaturated, and to prevent disturbance of the electrospraying, it is important to use a relatively low speed, which in our experiments is 270 mm/s (the plug-flow speed at the glass tube exit). The ES needle is held at a positive high voltage supplied by a high voltage amplifier (Matsusada AMS-10B2-LC) configured as a DC high voltage power supply (HVPS). A perforated brass plate (120 mm diameter), or backplate, surrounds the ES needle and is electrically connected to it, to create a more uniform electric field in the spray region. The distance between the back plate and the tip of the ES needle is 20 mm. For safety, a resistor R (200 MOhm) is placed between the HVPS and the needle, as shown in Fig. 1. Consequently, the voltage (electrical potential) provided by the power supply is not the same as that reaching the needle, referred throughout as needle voltage. The latter, determined by means of a HV probe (not shown) (Testec TT-HVP-40, 1 GΩ), typically varied between 5 and 10 kV. The collector plate is virtually held at Earth-ground, as it is connected to a handmade calibrated nano-ammeter, whose output voltage (proportional to the electrospray current collected on the plate, I_{exp} is recorded at 20 Hz. The uncertainty in the current is set by the repeatability of the average current, which we estimate at less than ±2 nA. The distance between the needle tip and the collector plate (H in Fig. 1) can be adjusted by moving the needle assembly up and down with the help of three nylon posts that are inserted in the cover, held at about 30-40 mm. This choice of distance is based on the idea of using a reasonably low needle voltage while still allowing the droplets to dry up sufficiently.

The substrates for particle deposition were made of P-type (100) silicon wafer doped with boron (Siltronix, 500-550 µm thickness and 1–50 Ω cm resistivity), previously cut into small squares of a desirable size (typically a few cm on a side, but not necessarily square-shaped). These small pieces were placed on a metal strip and were then slid under the spray for a few seconds to collect particles from the drying droplets. For this operation, the strip was inserted through one of two slits under the chamber (see Fig. 1), and, after collecting particles, taken out of the chamber through the opposite slit. The deposition time ranged between 10 and 30 s, and this was long enough to obtain sufficient particles for further analysis but avoid particle overlaps.

2.3 Scanning electron microscopy (SEM)

The samples were stored in a plastic petri dish and normally imaged on the same day or the next by a scanning electron microscope (Fei Quanta 600 ESEM) to study the particles' morphology and size. The silicon piece containing the deposit was cut with a diamond pen (if it is required) and then stuck on a carbon tape and placed in an aluminum stub. The samples were gold-coated at 30 mA for 60 or 90 s (~5-14 nm) in a sputter coater (either a Quorum Q150R ES or a Quorum Q150T S plus). Pictures of different magnifications were taken at different positions on the depositions (commonly center or middle zone). Most of the images shown here have been enhanced for brightness and contrast.

Each particle size was obtained using an image analysis software (Sigma Scan Pro 5.0, Aspire Software International Ashburn, VA). The statistics on the particle size for each condition were based on 70 to 280 particles (N) from various SEM images. For spherical particles, we used Feret diameter (d_F) as a characteristic dimension, whereas for particles with non-spherical morphology we consider the projected area-equivalent diameter (d_S), which is defined as the diameter of a circle having the same projected area as the particle.

2.4. Focused ion beam field-emission scanning electron microscopy (FIB-FESEM)

Cross-sections of CUR and CUR-loaded PVP particles were obtained by a dual beam microscope (FEI company Scios 2), equipped with a gallium focused ion beam (FIB). For the particles milling, the ion beam energy and the probe current were 30 kV and 1 nA, respectively. We imaged the

cross-section of some representative particles for each selected sample, which were previously gold coated at 30 mA for 90 s (~14 nm estimated coating thickness) in a sputtering machine (Quorum Q150T S plus) and covered in situ with platinum before milling.

2.5. Fourier Transform Infrared Spectroscopy (FTIR)

The infrared spectra were obtained using a 6700 Jasco FT/IR spectrophotometer. Electrosprayed particles with a different drug to polymer mass ratios were deposited on small pieces of silicon wafers for about ten minutes and analyzed directly. In addition, we analyzed the raw materials and a physical mixture of both (1:1 weight ratio). The scanning was performed at a spectral resolution of 4 cm^{-1} and 32 scans between 4000 and 400 cm^{-1}.

2.6. X-Ray diffraction (XRD)

X-ray diffraction measurements were made using a Siemens D5000 diffractometer (Bragg-Brentano parafocusing geometry and vertical θ-θ goniometer) fitted with curved graphite diffracted beam monochromator, incident and diffracted-beam Soller slits, a 0.06° receiving slit and scintillation counter as a detector. The angular 2θ diffraction range was between 5 and 40°. The data were collected with an angular step of either 0.03° or 0.05° at 20 or 3 s per step and sample rotation, respectively. A low background Si (100) wafer was used as a sample holder. Cukα radiation was obtained from a copper X-ray tube operated at 40 kV and 30 mA. For the raw materials (CUR and PVP) and their physical mixture (1:1 weight ratio), a small amount of powder was placed on the holder and flattened before the scan. Electrosprayed particles were analyzed directly on their Si collection substrates.

3. Results and Discussion

3.1. Electrospray stability at low flow rates

We first analyze the keys to achieving stable and robust electrospraying from our CUR-PVP systems at the low flow rates necessary to make small droplets. To verify the existence of the Steady Cone-Jet (SCJ) mode we imaged the Taylor cone (TC) and monitored the electrical current transferred to the collector plate. The current versus flow rate relationship is unique to each mode of liquid

atomization, and its monitoring over time is a robust way to identify instabilities [47,80]. These approaches have been validated in the literature in idealized experiments using pure solvents or dilute solutions, for example, ethylene glycol and water [28,36,81,82].

Under stable conditions (SCJ mode), we have thoroughly studied the influence of solution composition and process variables on the particles' sizes. Table 1 collects this information for our low-RH experiments, as well as the physicochemical properties of the polymeric solutions. This table also reports the theoretical predictions based on models developed for simple fluids [27] for the droplet size, the electrospray current, and the minimum flow rate for stability of the SCJ mode for each solution [78], below which flow rate the liquid meniscus undergoes intermittent jetting, and the droplet size distribution is suboptimal [47].

To obtain small droplets and sustain small flows with these solutions, one must satisfy two requirements: (1) The use of liquid flow rates near the minimum flow rate of stability, and (2) the use of a gas coflow saturated with solvent-vapor to prevent the cone drying when electrospraying concentrated solutions at low flow rates.

To obtain a first guess of the minimum flow rate compatible with stability, the theoretical minimum flow rate ejected in the SCJ mode, Q_{min}, was computed as a function of the solution properties for every solution. As proposed by Gañán-Calvo et al. [78] when the viscous forces are not strong enough to stall the jet emission, the minimum flow rate is scaled as:

$$Q_{min} = Q_0 \beta \quad (1)$$

$$Q_0 = \frac{\sigma \varepsilon_0}{\rho k} \quad (2)$$

Where σ is the surface tension of the solution, ρ its density, k its electric conductivity, and $\beta = {\varepsilon_i}/{\varepsilon_0}$ its relative electrical permittivity (dielectric constant), where ε_0 and ε_i are the electrical permittivity of vacuum and of the liquid, respectively. The condition of low viscosity is fulfilled by the inequality:

$$(\beta \delta_\mu)^{-1} < 1 \quad (3)$$

where $\delta_\mu = \left[\frac{\sigma^2 \rho \varepsilon_0}{\mu^3 k}\right]^{1/3}$ is the electrohydrodynamic Reynolds number, being μ the dynamic viscosity of the solution.

This simple computation of Q_{min} was useful as a starting point for selecting a flow rate suitable for operating in the SCJ mode. In our experiments we operated at flow rates which did not differ greatly from Q_{min} as shown in Table 1. We chose 0.75 µL/min as a common flow rate near the computed Q_{min} values, at which we could compare experiments with different solution compositions. In experiments with fixed composition, we studied the dependence on the solution flow rate of the electrospray current and particle size. In all cases, we ensured that we operated in the SCJ mode and that the process was stable by both monitoring the TC and the electrospray current.

Fig. 2 demonstrates the utility of monitoring the TC and the electrospray current, as the process control variables (needle voltage and flow rate) are varied versus time. As the flow rate is increased, the needle voltage is adjusted upwards in order to maintain a similar TC shape, as shown (Fig. 2a, 2b). Fig. 2c shows the corresponding electrical current trace. Transients in the current trace are observed in response to adjustments in the control variables (flow rate and needle voltage), as expected. Otherwise, the steadiness of the electrospray current traces proves the stability of the electrospraying process over the range of liquid flow rates tested, from 0.75 to 4 µL/min. Beyond 5 µL/min for this solution, we could not establish a stable TC and the electrical current started to fluctuate (data not shown).

The second requirement that must be satisfied to sustain the low flows needed to obtain small droplets, especially with concentrated solutions, is the prevention of the drying of the TC by means of a coflow gas saturated with solvent vapor (Fig.1) [16,50,51]. Fig. 3 illustrates the time sequence while electrospraying 5C-5P solution at a constant liquid flow rate (0.75 µL/min). Initially, when the coflow gas is on, the TC was stable (Fig. 3a) and the measured electrospray current was 28 nA. The coflow was turned off after 140 s and the cone started to dry up (Fig. 3b) and became unstable until the jet disappeared (Fig. 3c, 3d). During this unstable period, the electrospray current dropped from 28 to 4 nA (in the range of our instrument resolution). After 190 s, the coflow gas was turned on again, after

which the TC recovered (Fig. 3f) after a transient which involved elongation (Fig. 3e) and the expelling of a large liquid mass.

To obtain a stable cone with least concentrated solutions, the coflow gas was not necessary (at least for the duration of our experiments); however, we still used the coflowing gas to minimize evaporation from the TC, so that we can assume that the initial solute concentration remains constant in the region where the jet forms (which is a necessary condition for the theoretical expressions to be valid).

Note that the average gas speed of 270 mm/s is low compared to the liquid jet speed, which is several tens of m/s, estimated from mass conservation as $4Q/\pi d_J^2$, where d_J can be estimated as $d_D/1.89$ [9]. Keeping a low coflow speed reduces perturbing the jet. In addition, increasing the coflow speed often has the opposite effect to the one intended, by enhancing solvent evaporation from the liquid/gas interface, driven by the increased vapor concentration gradient at the boundary layer next to the liquid-gas interface.

3.2. Particles with low curcumin content

First, we focus on the main effects of the polymer concentration and solution flow rate on the size and morphology of the particles. Ethanol was used as it is a good solvent for PVP, but not for CUR; nonetheless, in these solutions we admitted a low CUR content of 0.1%. Fig. 4 shows the morphology of the collected particles from different PVP concentrations and flow rates, all sprayed at dry ambient conditions (RH < 5%). Within each collected sample, the larger particles were of similar size. This strongly indicates quasi-periodicity in the droplet formation during the breaking up of the EHD jet (Fig. 5), corresponding to the Plateau-Rayleigh jet breakup mechanism [47]. The size of such *main particles* (particles arising from dried *main droplets*) increases from ~0.5 μm at the lowest PVP concentration (1% w/w) at 0.75 μL/min (Fig. 4a1, 4b1) to ~0.9 μm for the particles produced at higher concentrations and higher flow rates (Fig. 4a2, 4a3 and 4b3).

Fig. 4b shows the dependence of the particles with the infusion flow rate Q for solution 0.1C-3P (0.1% CUR, 3% PVP). As the liquid flow rate varied from 0.75 to 3 μL/min, the particle size mean

increased from 0.46 μm to 0.78 μm, qualitatively in accordance with the trend expected for the electrospray droplets (predicted theoretically in Table 1). The interpretation of the particle size mean in Fig. 4a is more complex because two additional factors are intervening besides flow rate Q: solution conductivity k, and solute concentration C. These dependencies are analyzed and discussed later below (Section 3.5).

Besides the *main particles*, smaller particles were also obtained from solutions with 1, 3 and 5% w/w PVP; (see Fig. 4a, 4b). These smaller particles are the result of Coulombic instability of the main droplets happening in flight as they evaporate in the spray plume region (Fig. 5). Coulombic instability (also called electrocapillary instability) happens during the droplet drying at a critical droplet radius (theoretically predicted by Rayleigh as, $r_{Ray} = q^2/(64\pi^2\varepsilon_0\sigma)^{1/3}$), when the droplet electrical surface stress exceeds the droplet capillary stress [83,84]. The instability evolves by development of one or two jet emissions [85,86], which can either solidify leaving filaments, or, if the solute is dilute enough, develop capillary waves leading to breakup into nanodroplets by the Plateau-Rayleigh instability [16,17,87]. The second scenario is called "Coulomb fission" or "Coulomb explosion", and the particles resulting from the progeny droplets are often called "progeny particles". It is important to distinguish these from the particles formed from the satellite droplets produced in the primary breakup of the EHD jet (Fig. 5) [16]. Fig. 4a shows this transition from the Coulomb fission regime at 1, 3 and 5% PVP, and the filament forming regime at 8% PVP; whereas at 10% PVP only a few short filaments are present. In this scenario, the droplets develop an outer layer (shell) which is elastic enough to resist nanojet emission; in other words, the droplets remain electromechanically stable at all radii. In all scenarios, a shell eventually formed on the main droplets, which is not rigid and eventually buckled into red-blood-cell like shapes [16].

With this set of experiments, we have learned that, for some solution concentrations (between 8 and 10% PVP), it is possible to produce monodisperse globular submicron particles with low curcumin content.

3.3. Particles with high curcumin content

The next step was to increase the curcumin loading, as this would be relevant for applications. However, ethanol is a good solvent for PVP [60,88], but not for CUR. Since curcumin is highly soluble in acetone [63,89], after some trial and error, we found 1:1 v/v ethanol/acetone to be a suitable solvent mixture for dissolving both CUR and PVP at significant CUR-PVP ratios, higher than previously studied in the electrospray literature [76,77]. We then systematically studied the particles' size and morphology versus solute weight concentration in the electrosprayed solution, first by varying the PVP weight concentration between 0 and 5% at a constant 5% CUR concentration, and then by varying the CUR weight concentration from 0 to 7.5%, at a constant 5% PVP concentration. Additionally, we investigated the inner/internal structure of the main particles produced using FIB-FESEM for some of these compositions, to get hints on the evaporation history of the droplet.

Fig. 6 shows the particles' shapes and particle size distribution histograms at varying PVP concentration but constant CUR amount (5%) in the solutions, all electrosprayed at the same Q (0.75 μL/min). At the zero-PVP condition the particles were spherical. However, as the PVP concentration increased to 1%, and later to 2.5%, the particle shape evolved from spherical to corrugated. The average particle size increased from 0.44 μm to 0.56 μm, and to 0.69 μm, respectively. A further increase in polymer concentration from 2.5 to 5% (Fig. 6c, 6d)) resulted in a small increase in particle size (to 0.75 μm). These particle size increases are mainly due to two causes: (1) the increase in solute concentration, despite the predicted droplet size decreases (Table 1), and (2) the earlier formation of the solid shell with increasing polymer concentration, as revealed by the loss of particle sphericity. There is an additional consideration for the highly non-spherical particles: When the particles tend to rest on their "flatter" sides, maximizing contact with the substrate (as will be shown later with FIB-FESEM) their projected area-equivalent diameter (d_S) will be slightly larger than their true orientation-averaged size.

Regarding the relics left from Coulombic instabilities, we find the same overall picture as was found with the ethanolic solutions previously: progeny particles formed at lower solute concentrations (solutions 5C-0P and 5C-1P) but were absent at PVP concentration above to 2.5%. When only CUR

is present, no filaments appear on the particles, whereas a little polymer (5C-1P) can stabilize the transient nanojet emitted during a Coulombic instability, resulting in some filamented particles.

Fig. 7 shows the effects on the particles and the particle size histograms when varying CUR concentration in the solutions at constant PVP amount (5%). Again, Q (0.75 µl/min) was used except for the most concentrated solution, which was not stable at this flow rate and was sprayed at 1.5 µL/min. As the CUR concentration was increased from 0 to 1%, the average particle size increased slightly [16].

Fig. 8 shows FIB-FESEM cross-sections of representative particles from selected conditions from Fig. 6 and Fig. 7. The insets show top views of each particle and where it was milled. Additional similar images of other particles from the same samples are shown in the Supplementary File (Fig. SI.1).

Fig. 8a shows that the curcumin-only (CUR) particles have a dense (void-free) internal structure. This morphology is expected when, during the droplet's drying history, the solvent evaporation flux is small compared to the solute diffusion flux from near the surface of the drop toward its center. A comparatively fast diffusion will tend to homogenize the solute distribution within the droplet [90–95]. While the droplet dries up, the solute enriches at the droplet's surface, thus solute precipitation would be expected to be initiated there, but this can happen very late in the droplet's evaporation history if the solute is very soluble. The faster evaporation of acetone is expected to enrich the droplet surface in ethanol, and thus to promote the precipitation of CUR first, due to its poor solubility in ethanol. Nonetheless, there is no evidence of early precipitation of CUR, as compact spherical shapes are formed (Fig. 8a) and the droplet is able to shrink to the Rayleigh limit radius and undergo Coulombic instability releasing progeny particles, as shown in Fig. 6a.

When a small (1%) amount of polymer was present in the electrosprayed solution the particles are still globular and with a smooth surface, but they have nano-cavities inside (Fig. 8b). At this low PVP concentration relative to CUR, the droplet evolution is similar to the case of CUR-only (Fig. 8a), with solute precipitation happening relatively late in the droplet's drying history, thus leading to small

spherical particles with a few voids. Nonetheless, the presence of polymer slows down the solute diffusion mass-transfer, and in the later stages of evaporation will result in a more viscous as well as stronger, more elastic structure. Consequently, droplet shrinking will slow down, and phase separation inside the droplet may occur resulting in solute-poor (solvent-rich) zones inside the particles which become nano-cavities in the latest stages of the drying.

When the PVP concentration in the sprayed solution is comparable to that of CUR (2.5 and 5%), the particle morphology becomes corrugated, as shown in Fig. 8c-f. Corrugation reveals the formation of a spherical shell which later underwent collapse. The formation of that shell is caused by significant polymer enrichment at the droplet surface during solvent evaporation, due to the slow polymer diffusion rate. This polymer-rich shell probably evolves from an early gel-like state to a consistent but deformable rubbery state, which eventually buckles and collapses under the pressure difference which develops across the shell caused by solvent evaporation, leading to a corrugated shape (Fig. 8c-f) [16]. The shell collapses fully, as the compact interiors of these particles reveal. Note that the transport of CUR by diffusion could also be slowed down due to hydrogen-bonding of the CUR to the PVP, as will be shown later.

To sum up, we were able to raise the CUR loading by using an ethanol/acetone mixture (1:1 v/v). At high enough solute concentrations (7.5% in total), the particles are monodispersed without filaments or progeny particles, demonstrating the absence of Coulombic instabilities during drying. At this low RH, the CUR-PVP particles are deflated shells with compact, void-free interiors, except for low PVP content, where we found more spherical particles, sometimes with nanocavities.

3.4 Effect of relative humidity on particle morphology

We previously showed that, for the case of water-insoluble polymers, relative humidity (RH) in the spraying ambient strongly influences the particle formation process, by driving polymer precipitation through non-solvent interactions [16]. Here we have a water-soluble polymer (PVP), and a water-insoluble compound (CUR), a combination for which the influence of RH on particle

morphology has not been studied. Therefore, we investigated whether the particle morphology can be tuned by changing the RH in the CUR/PVP/ethanol/acetone system.

For the solution containing only PVP (0C-5P) a continuous film was observed when we electrosprayed under humid conditions (Supplementary File, Fig. SI.2). Wet collections were also reported by Rezeki et al. [57] when electrospraying mixtures of PVP and mangosteen pericarp extract (MPE) at RH under 50%, at zero and low MPE/PVP ratios. On the other hand, in our experiments, all the CUR-PVP mixtures led to particulate structures.

Fig. 9 shows the morphologies obtained with different CUR-PVP compositions after humidity was increased from low RH (< 5%), shown in Fig. 6 and 7, to (a) intermediate RH (35-45%), and (b) high RH (60-70%). The solution with only CUR (5C-0P), which at low RH (Fig. 6a) produced spherical main particles surrounded by progeny particles, at intermediate (Fig. 9a1) also produced spherical particles (although not completely dried) without progeny particles. High RH led to larger and porous particles (Fig. 9b1), also without progeny particles. Similar tendencies were found for the next composition (5C-1P), where CUR still dominated, shown in the sequence of Fig. 6b, Fig. 9a2, and Fig. 9b2. These observations suggest that water taken up by the droplet from its surrounding ambient encouraged the precipitation of the (water-insoluble) CUR, happening earlier in the droplet's history as the RH increased. At high enough RH (Fig. 9b1 and Fig. 9b2), more water can be absorbed, or even condensed onto the droplet surface with nanodrops acting as templates, leading to the formation of small cavities at the particle's surface (possibly connecting with cavities in the particle's interior). Particle porosity due to high RH is consistent with earlier studies; however, with water-insoluble polymers (i.e., polystyrene) [16,52].

For solution 5C-5P (Fig. 6d, Fig. 9a3, Fig. 9b3), the particle morphology was corrugated and free of progeny particles in all three humidity cases. Smaller CUR concentration in the solution (1C-5P), at both low (Fig. 7b) and intermediate RH (Fig. 9a4), led to corrugated particles, although at intermediate RH there were fewer filamented and progeny particles. At high RH, as shown in Fig. 9b4, this solution interestingly produced samples with smaller, spherical and smooth particles, without progeny particles. This can be explained as follows: at high enough RH, solvent composition not only

changes due to solvent fractionation by the faster evaporation of the more volatile acetone, but water can also get into the droplet, changing the solvent composition. PVP is very soluble in water, meanwhile the aqueous solubility of CUR is also enhanced by the presence of PVP [63,96,97]. Thus, both solid components can remain soluble and undergo molecular diffusion toward the droplet's center without precipitating; whereas they precipitate at low RH forming shells which collapse (Fig. 7b). At the same time, a slight amount of CUR (1C-5P) reduces the water affinity of the mixture, enough to stabilize the particle surface, preventing the formation of the wet films which were encountered with solutions without CUR at high RH (Supplementary File, Fig. SI.2). The absence of Coulombic instabilities at higher relative humidity levels could be explained by the increase in surface tension due to the water uptake.

The preceding discussion reveals that the problem is rich and much too complex to be completely developed in the current article. Nonetheless, this set of experiments demonstrates that relative humidity, besides solution composition, strongly influences the morphology of CUR-PVP particles from ethanol-acetone solutions, with the main effect of preventing Coulombic instabilities (e.g., solutions 5C-0P, 5C-1P, and 1C-5P). An interesting practical outcome was the formation at elevated RH of progeny-particle-free samples with submicron highly spherical particles with a 1:5 CUR-PVP mass ratio (solution 1C-5P). These are the smallest and most monodispersed composite CUR-PVP particles (with a relevant curcumin loading of 16.7%) obtained in this work, with average particle diameter of 0.50 μm and SD of 0.04 μm (N=200).

3.5. Scaling laws predictions versus data

We have also investigated the connections between our experimental data and the predictions from theoretical models of the cone-jet formation process. Such models, based on first principles, describe the steady state emission of the liquid EHD jet sustained by the electrostatic forces due to the TC [47]. They predict the jet size, thus droplet diameter d_D (as jet diameter times 1.89, the well-known Rayleigh-Plateau factor) and the electrical current I. A simplifying assumption, confirmed by experiment, states that electrostatic parameters (electrodes sizes and shapes, and their voltages) do not

enter the picture; thereby reducing the set of independent parameters to the liquid flow rate Q and mechanical and electrical liquid properties [98].

We consider the predicted scaling laws proposed by Gañán-Calvo et al. for d_D and I [27]:

$$\frac{d_D}{d_0} = \left(\frac{Q}{Q_0}\right)^{0.5} \quad (4)$$

$$\frac{I}{I_0} = 2.6\left(\frac{Q}{Q_0}\right)^{0.5} \quad (5)$$

Where Q_0 is defined by Eq. (2), and the other two normalizing factors d_0, I_0 are the following functions of the air permittivity ε_0 (taken as that of vacuum, i.e., 8.854×10^{-12} F/m) and the liquid properties: surface tension σ, density ρ, electrical conductivity k (but not viscosity).

$$d_0 = \left(\frac{\sigma\varepsilon_0^2}{\rho k^2}\right)^{\frac{1}{3}} \quad (6)$$

$$I_0 = \sigma\left(\frac{\varepsilon_0}{\rho}\right)^{0.5} \quad (7)$$

In these expressions (Eq. (4) and Eq. (5)), the exponent 0.5 is often fulfilled quite precisely across different compositions, especially for the current. However, the prefactors (2.6 and 1.0) are only global averages of prefactors which vary significantly across the many independent experiments. Note that these scaling laws apply to Newtonian fluids, and they have been verified only with simple fluids such as pure solvents or solvents with a small content of electrolyte, such that only the electrical conductivity is affected by this solute. Note also that neither the viscosity of the liquid nor its electrical permittivity are involved in these expressions. In our computations of I_0, d_0 and Q_0 we have assumed that the surface tension of the CUR-PVP ethanolic solutions is close to that of the pure ethanol (taken at 20 ºC, i.e., σ = 0.02239 N/m), whereas the surface tension of the solutions of CUR-PVP in ethanol/acetone was considered close to that of the solvents' mixture at 20 ºC [99]. (See Supplementary File, section SI.4).

3.5.1. Electrospray current

Fig. 10 shows our experimental electrical current data (Table 1) plotted in the nondimensionalized variables of Eq. (5). The empty symbols correspond to the ethanolic solutions,

and the filled symbols represent the ethanol/acetone-based solutions. Note that the abscissa (Q/Q_0=$Q\rho k/(\sigma\varepsilon_0)$) increases not only with Q but with k as well, which has a notable spread (Table 1). The data are well-fitted by a power law with a power very near the theoretically predicted value of 0.5 (Eq. 5). Unexpectedly, the prefactor (1.728) is significantly lower than the global value given in Eq. (5) (2.6), but this difference is well within the spread of the data for simple fluids [27]. Another unexpected result from Fig. 10 is the slight upward curvature in the data, suggesting a dependence of the exponent with Q/Q_0. However, this could be questioned if we consider that the three lowest current values have the highest error (at least +/- 10%). A fitting ignoring these values gives a larger exponent of 0.62, which is reasonably close to 0.5. More extensive experiments would be needed to confirm this trend.

Whether these non-idealities (prefactor and curvature) are caused by the presence of the solutes in our solutions or not remains a question for further study. Regardless, the important conclusion from Fig. 10 is that the tested scaling law for the electrical current applies quite well to the CUR-PVP solutions of this study. Therefore, the model and, consequently, its predicted scaling law for the droplet diameter is also expected to apply to our study. This is developed in the next section.

3.5.2. Droplet and particle sizes

Our goal is to evaluate the applicability of the scaling law for the droplet size of Eq. (4) to our system. To relate the particle size to the droplet size one must consider both the initial solute concentration and the particle's shape. If the particles have a very similar shape, the particle and the droplet sizes can be expressed as proportional to one another:

$$d_P = \mathrm{A}\ d_D \tag{8}$$

where

$$\mathrm{A}=\left[\frac{C\rho}{(\rho_{bulk}(1-\Phi))}\right]^{1/3} \tag{9}$$

where C is the solute mass concentration (by weight) in the initial solution, ρ the initial solution density, ρ_{bulk} the bulk density of the solute (in the dry particle), and Φ a porosity parameter for the

dry particle (connecting the particle diameter to the diameter of the mass-equivalent compact sphere). In sum, the dependence of the particle size versus initial polymer concentration, in the case when similarly shaped particles are made (thus having similar Φ), is expected to scale as follows:

$$d_P \sim \left[\frac{c\rho}{\rho_{bulk}}\right]^{1/3} d_D = C^{1/3} \left(\rho/\rho_{bulk}\right)^{1/3} (\rho\varepsilon_0/\sigma k)^{1/6} Q^{1/2} \qquad (10)$$

where Eq. (4), Eq. (2) and Eq. (6) have been considered. Note that this also assumes low or negligible mass loss by Coulombic instabilities, a condition which is typically fulfilled.

Independently, by setting the porosity parameter to 0 in Eq. (9), we can also express the compact-sphere equivalent diameter (d_{CS}) as a function of the initial droplet diameter:

$$d_{CS} = C^{1/3} (\rho/\rho_{bulk})^{1/3} d_D = C^{1/3} \left(\rho/\rho_{bulk}\right)^{1/3} (\rho\varepsilon_0/\sigma k)^{1/6} Q^{1/2} \qquad (11)$$

where d_D is the initial droplet diameter. The bulk density of the particles made of both components was estimated from the bulk density of the individual compounds (See Supplementary File, section SI.5). The compact-sphere equivalent diameter should always be below or equal to the measured particle diameter, and their difference can be useful to assess porosity or morphology and thus hint on particle drying mechanism.

We first analyze the particle size data in Table 1 for the ethanolic solutions. In this case, the addition of polymer (with a tiny constant amount of CUR) changed the electrical conductivity by a factor of about 4, and we varied the flow rate threefold (Table 1). Since the particles are similarly shaped, as can be seen in Fig. 4, we can test the prediction of Eq. (10). This is shown in Fig. 11, where we find that the particle diameters follow a linear trend. The predicted trendline, however, is only in partial agreement with Eq. (10) since the ordinate at the origin is finite (not very small compared to the data values). Nonetheless, the high correlation of these points indicates that the assumptions behind Eq. (10) are fulfilled to a great degree. This includes the implicit scaling law, particularly the dependence on k and Q (which vary in the data set). Note that the figure involves liquid solutions varying in the solute concentration by a factor of more than 10. The fact that the data points all cluster tightly around the trendline suggests the absence of any rheological effects in the jet formation or

breakup processes. This means that, throughout the jet formation and breakup, these solutions are in a dilute regime where the polymer chains are not interacting to any significant extent. Additionally, we should note that the large variability in the droplet sizes is because the proportionality constant A in Eq. (9) is different across different points.

For the ethanol/acetone-based solutions we present the data differently, as we observe significant variation in particle shapes depending on the solute composition (Fig. 6 and Fig, 7). In Fig. 12 we compare the particle diameters for otherwise the same flow rate, while varying the PVP concentration at constant CUR concentration (Fig. 12a) or while varying the CUR concentration at fixed PVP concentration (Fig. 12b). We also show the predicted droplet size d_D and the equivalent CS diameter d_{CS}.

For Fig. 12a the measured particle size follows the opposite (increasing) trend of that of the calculated compact sphere diameter, as the particles' shapes change from compact spherical to corrugated, with increasing PVP concentration, as shown in Fig. 7. In the case of the more spherical particles (Fig. 8a and Fig. 8b) the measured particle size and predicted CS size are in close agreement (Fig. 12a). Whether this surprisingly close agreement between the predicted and measured compact diameter is a coincidence or reflects a close agreement with the scaling laws remains a question. More spherical particle shapes are expected when the diffusion of solute species in the droplet is fast (compared to its drying), and this may be occurring for CUR due to its small molecular weight. For the case of 5% CUR, 1% PVP the small difference between the particle and CS diameters could perhaps be attributed to the presence of nano-cavities. As the polymer concentration increases further, the particle size separates more and more from the predicted CS size, as the particles become more corrugated.

In Fig. 12b showing the dependence with CUR concentration, all the particles are corrugated (due to the presence of the polymer) so we expected a more constant difference between the computed CS and the measured particle sizes than in Fig. 12a. Still, the particle size jumps up between the CUR concentrations of 1% and 2.5%, while the predicted CS diameter is increasing slowly. The shape differences visually do not explain this jump; suggesting that the jump in particle size corresponds to

a jump in initial droplet diameter between these concentrations (for a currently unknown reason). As in the ethanol case (Figure 11), the droplet forms at (or near) the initial solution composition, as the jet is protected from evaporation. Nonetheless, in the ethanol-acetone case, for the compositions with higher concentrations of both CUR and PVP (Fig. 12b), we cannot rule out effects from viscosity and/or rheology in the jet formation and breakup, which might arise by specific interactions (H-bonding) between the two solutes, and which would result in larger initial droplet sizes relative to the predictions from the scaling laws. All in all, the main message from Fig. 12 is that the particle size falls between the initial droplet and CS sizes, as expected, and therefore that the scaling laws are a powerful instrument to approximately predict the CS and particle sizes, where CS is expected to be a lower bound estimate when particle corrugation and Coulombic instabilities are considered.

3.6. Solid state characterization: FTIR and XRD

The FTIR spectra shown in Fig. 13 compares the molecular structures of the different CUR-PVP nano-formulations to the as-purchased (raw) components and their physical mixture (at 1:1 weight ratio). Raw CUR gave its characteristic spectrum, with peaks for the stretching vibrations of its functional groups at 3507 cm^{-1} (-OH), 1626 cm^{-1} (C=O), 1601 cm^{-1} (benzene ring), 1506 cm^{-1} (C=O and C=C), 1275 cm^{-1} (C-O) and 1426 cm^{-1} for C-H bending vibration [76,100,101]. The PVP spectrum is also as expected, with a broad peak with a maximum at 3410 cm^{-1} which corresponds to the stretching vibration of -OH groups, and peaks at 2950 cm^{-1} (C-H stretching vibration), 1647 cm^{-1} (C=O bending vibrations), 1421 cm^{-1} (C-H bending vibrations) and 1286 cm^{-1} (C-N stretching vibrations) [76,101]. The spectrum of the physical mixture of PVP and CUR is a superposition of those of the raw components without any additional peaks, proving that no chemical reaction took place between CUR and PVP, as previously reported [89,97]. The spectrum of the electrosprayed CUR-only nanoparticles (from solution 5C-0P) contains the main characteristic peaks of raw CUR, as expected [77,102]. The sharp peak observed in the unprocessed curcumin at 3507 cm^{-1} disappeared in the electrosprayed CUR-PVP composite samples This change has been seen in other works, with CUR-PVP composite particles prepared by either electrospray or other liquid atomization methods [76,89,96,97,101], where it has been attributed to hydrogen bonding between O-H functional groups of the CUR and C=O groups

of the PVP. According to Matos et al. [89] and Kaewnopparat et al. [97], the hydrogen bonding between both components might explain the inhibition of crystallization of CUR, thus improving its aqueous solubility. Besides this, there are no other shifts or broadening of the characteristic peaks of the two components in the electrosprayed samples.

Fig. 14 shows the X-ray diffraction patterns of raw CUR and PVP, their physical mixture, and the electrosprayed CUR-PVP particles. Raw curcumin exhibits peaks at 7.95°, 8.95°, 12.25°, 14.53°, 17.30°, 18.20, 23,45°, 23.85°, 24.65° and 25.70° which corresponds to the planes of (100), (002), (010), (102), (-204), (004), (-115), (-215), (020) and (-125) [103]. This diffraction pattern is characteristic of the polymorphic form I (keto form) of crystalline curcumin [75,104]. The absence of diffraction peaks in the unprocessed PVP pattern confirms the amorphous nature of the polymer, with two weak broad halos centered on 13° and 21° [76,105], whereas the diffraction pattern of the physical mixture (CUR-PVP 1:1) is dominated by the curcumin crystallinity peaks. On the other hand, the diffractograms of the electrosprayed particles are in halo patterns, without any crystalline CUR peaks, revealing that the CUR was in an amorphous state, both in the presence and absence of PVP. This can be attributed to the rapid droplet drying process, which precludes the formation of CUR nuclei [106], and for particles containing PVP, also to the hydrogen bonding between the polymer and the CUR, verified by the FTIR analysis. The absence of crystallinity in the XRD is also consistent with the presence of globular shapes, free of any visible crystal facets. Images of raw CUR powder, on the other hand, showed needle-like shapes (see Supplementary file, Fig. SI.3)

4. Conclusions

The periodic liquid jet breakup in electrospray cone-jets by the Plateau-Rayleigh instability has allowed the stable production of monodispersed curcumin (CUR) loaded polyvinylpyrrolidone (PVP) particles with sizes under 1 μm. These have been prepared with different drug to polymer ratios, using two different solvent systems, ethanol and ethanol/acetone (1:1 v/v). We have focused on achieving stable spraying in the Steady Cone-Jet (SCJ) mode, at liquid flow rates close to the minimum value, which led to the smallest particle sizes. We found that this minimum flow rate was reasonably close to the theoretically predicted value valid for simple fluids. We have shown the importance of

preventing the drying of the Taylor cone by using a gentle gas flow (nearly) saturated in solvent-vapor, in order to maintain the spraying mode in the SCJ mode while operating at such low flow rates with volatile solvents.

With ethanol as solvent, the CUR loading was very low (0.1%) due to its limited solubility. With increasing PVP concentrations, the particle morphologies progressed from globular main particles surrounded by progeny nanoparticles to filamented main particles (reflecting that the droplets underwent Coulombic instability (CI) events), and to globular main particles almost without filaments (indicating the disappearance of CI events). With ethanol/acetone (1:1 v/v) as solvent, the CUR loading could be greatly increased, obtaining globular particles with corrugated morphology, without signs of CIs when the total solute concentration in the electrosprayed solution was high enough.

FIB-FESEM analysis of particles made from the CUR/PVP/ethanol/acetone system, revealed mostly void-free interiors. Knowledge of this internal structure has been used to propose different mechanisms for particle formation. Whereas at lower PVP concentrations we found small spherical particles which formed from a thicker shell, at higher concentrations corrugated shapes were collected, resulting from the collapse of thinner spherical shells.

The effects due to the ambient relative humidity (RH) on the particles' morphologies were studied for the CUR/PVP/ethanol/acetone system, and were found to depend strongly on solution composition. While no apparent changes were noted for the higher solute concentration case (5% CUR - 5% PVP), RH had a significant influence on particle morphology at both lower PVP and CUR concentrations. When we lowered the polymer (PVP) concentration, raising the RH resulted in more irregular particles. Lowering the CUR concentration had the opposite effect: higher RH resulted in increasingly spherical particles. In both cases there is a clear reduction in Coulombic instability events due to the presence of water (in the droplet). This demonstrates that the theoretical analysis of the problem is quite complex and that the presence of even a relatively small amount of the water-insoluble component (1% CUR versus 5% PVP) can result in big morphological changes, by altering the solutes' precipitation dynamics.

FTIR analyses of the electrosprayed samples confirmed the formation of hydrogen bonds between PVP and curcumin, without further chemical modification of the chemical structure of the molecules, whereas XRD confirmed the absence of curcumin crystallinity in our particles.

Finally, we show that the theoretical predictions of electrical current and droplet size from well-established cone-jet physics models developed for simple fluids are also applicable to our more complex liquid solutions. For example, the particle sizes are consistently close to and larger than the predicted dry residue diameter.

In sum, this work demonstrates that consistent particle morphologies by electrospray requires the conditions that sustain stable Taylor cones with Plateau-Rayleigh jets. A diversity of particle morphologies is found with mixed solutes that have different transport (diffusivity) and thermodynamic (solvophilic) behavior, in this case PVP and CUR. It is possible to remove the undesired effects on morphology arising from Coulombic instabilities of the drying droplets (filaments, and also progenies) by carefully choosing the atomized liquid composition and the process variables. In this way, we were able to produce amorphous CUR-loaded PVP quasi-monodisperse submicron particles, which could be an interesting model for drug delivery or biomedical applications.

Acknowledgements

Prof. Jordi Grifoll (Universitat Rovira i Virgili, Spain) is thanked for fruitful discussions. This research has been funded by grant PGC2018-099687-B-I00 from the Spanish Government through MCIN/AEI/ 10.13039/501100011033 and “ERDF A way of making Europe”. Financial aid from the Catalan Government through grant 2021SGR-00978 (AGAUR) is also acknowledged. E. Barbero acknowledges financial support from Spanish Government scholarship BES-2016-077914 (MINECO/AEI/FEDER, UE).

Figure Captions

Fig. 1. Electrospray (ES) chamber setup with main components. Inset: schematic of coflow tube and ES needle (metal capillary) with stable Taylor cone and electrohydrodynamic (EHD) jet. The blue arrow represents the solution flow, and the red arrows represent the solvent-saturated nitrogen coflow. R is a resistor for safety (see text).

Fig. 2. Stability of electrospraying process at different solution flow rates, Q, (from 0.75 to 4 µL/min) when electrospraying solution 1C-5P (Table 1) at RH < 5%. Needle voltage traces and solution flow rate versus time (a), snapshots of stable Taylor cones (b) and electrospray current versus time (c).

Fig. 3. Importance of the coflow gas (red arrows) on the Taylor cone stability for a concentrated solution (5C-5P) at low RH (< 5%). Time sequence of the cone drying (b-d) and recovery (e-f), when turning off and back on the solvent-vapor coflow, gas speed 270 mm/s. Constant liquid flow rate (0.75 µL/min) and needle voltage (4.8 kV) except (a) (4.6 kV).

Fig. 4. Particle morphologies from ethanolic solutions at varying concentrations of PVP (a), and different solution flow rates Q (b). In (a) Q varied somewhat from 0.75 µL/min (a1) to 1.5 µL/min (a2, a3) and to 1.0 µL/min (a4). All solutions contain a low (0.1% w/w) concentration of curcumin. RH < 5% inside the chamber. All scale bars are 1 µm.

Fig. 5. Schematic representation of droplet generation by electrospray with varicose jet breakup (or Plateau-Rayleigh mechanism) and Coulombic instability scenarios. The solvent-saturated gas coflow protects the jet region from drying and water-uptake (from ambient moisture when present).

Fig. 6. Top: SEM images of the CUR loaded PVP particles at increasing PVP concentration in the electrosprayed solution ([PVP]), at fixed (5% w/w) CUR concentration ([CUR]). Solvent: ethanol/acetone (1:1 v/v). Liquid flow rate was 0.75 µL/min and RH < 5%. The insets show magnifications of these particles. Scale bars: 1 µm. Bottom: corresponding particle diameter histograms, with the average Feret diameter $< d_F >$ (for 5C-0P) or the average projected area-equivalent diameter $< d_S >$, the standard deviation SD, and the number of sized particles N.

Fig. 7. Top: SEM images of the CUR loaded PVP particles at increasing mass CUR concentration in the electrosprayed solution ([CUR]), at fixed (5% w/w) PVP concentration ([PVP]). Solvent: ethanol/acetone (1:1 v/v). Liquid flow rate is 0.75 µL/min, except in (d) 1.5 µL/min, RH < 5%. The insets show magnifications of these particles. Scale bars 1 µm. Bottom: corresponding particle diameter histograms, with the average Feret diameter $< d_F >$ (for 0C-5P) or the average projected area-equivalent diameter $< d_S >$, the standard deviation SD, and the number of sized particles N.

Fig. 8. FIB-FESEM images of individual particles from different solution compositions (Table 1). Same liquid flow rate (0.75 µL/min), except (f) (1.5 µL/min), and low RH conditions (< 5%). The

insets are top views by SEM of the same particle before Pt coating and FIB milling, where the yellow dotted line indicates the approximate location of the imaged plane. Scale bars: 500 nm.

Fig. 9. Effect of relative humidity on the particles' morphology. SEM images of particles from selected solution compositions at: (a) Intermediate RH (35-45%) and (b) high RH (60-70%). The insets are magnifications of images of the same samples. The liquid flow rates were selected between 0.75 and 1.5 μL/min. Scale bars 1μm.

Fig. 10. Experimental data for the non-dimensionalized electric current I_{exp}/I_0 as a function of the non-dimensionalized flow rate Q/Q_0 for all the solutions and conditions tested (data in Table 1); I_0 and Q_0 defined in Eq. (7) and Eq. (2). Empty symbols: ethanol as solvent. Filled symbols: ethanol/acetone (1:1 v/v) as solvent.

Fig. 11. Particle size data analysis for the ethanolic solutions. The figure shows the predicted droplet diameter (black squares), the measured particle size (blue triangles) and the predicted compact-sphere diameter (red line) versus a particle size parameter predicted with the scaling laws of Eq. (10) and Eq. (11). Straight segments join the droplet diameter values to guide the eye; however, no analytical relationship is expected for the droplet size in this graph. The blue dashed line represents the least-squares fitting of the measured particle diameter. The large variability in the droplet sizes is expected as the proportionality constant A in Eq. (9) is different across different points.

Fig. 12. Comparison of the particle diameter from ethanol/acetone (1:1 v/v) solutions to the theoretically predicted droplet and compact-sphere diameters: (a) versus PVP concentration at a fixed 5% w/w CUR concentration, and (b) versus CUR concentration at a fixed 5% w/w PVP concentration (Table 1). Constant liquid flow rate at 0.75 μL/min. Low relative humidity conditions (RH<5%).

Fig. 13. Infra-red spectra of raw CUR and PVP powder, their physical mixture (PM) (1:1 w/w), and CUR-PVP electrosprayed nanoparticles from various solutions (Table 1). The grey bands correspond to the range of vibration energies of the O-H and C=O groups. The ES samples were electrosprayed at low RH, except for the bottom trace.

Fig. 14. X-ray diffraction patterns of raw curcumin (CUR) and PVP powder, their physical mixture (PM) (1:1 w/w), and CUR-PVP electrosprayed nanoparticles from various solutions (Table 1). Peak identification data (Miller indices and relative intensity) are shown for raw curcumin (from [103]).

References

[1] K. Okuyama, W.W. Lenggoro, Preparation of nanoparticles via spray route, Chem. Eng. Sci. 58 (2003) 537–547. https://doi.org/10.1016/S0009-2509(02)00578-X.

[2] E. Boel, R. Koekoekx, S. Dedroog, I. Babkin, M.R. Vetrano, C. Clasen, G. Van Den Mooter, Unraveling Particle Formation: From Single Droplet Drying to Spray Drying and Electrospraying, Pharmaceutics. 12 (2020) 625. https://doi.org/10.3390/pharmaceutics12070625.

[3] R. Vehring, Pharmaceutical particle engineering via spray drying, Pharm. Res. 25 (2008) 999–1022. https://doi.org/10.1007/s11095-007-9475-1.

[4] A. Sosnik, K.P. Seremeta, Advantages and challenges of the spray-drying technology for the production of pure drug particles and drug-loaded polymeric carriers, Adv. Colloid Interface Sci. 223 (2015) 40–54. https://doi.org//10.1016/j.cis.2015.05.003.

[5] R. Murugesan, V. Orsat, Spray Drying for the Production of Nutraceutical Ingredients-A Review, Food Bioprocess Technol. 5 (2012) 3–14. https://doi.org/10.1007/s11947-011-0638-z.

[6] R. Vehring, H. Snyder, D. Lechuga-Ballesteros, Spray Drying, in: Dry. Technol. Biotechnol. Pharm. Appl., Wiley-VCHVerlag GmbH& Co. KGaA, 2020: pp. 179–216. https://doi.org/10.1002/9783527802104.ch7.

[7] A. Bohr, J. Kristensen, M. Dyas, M. Edirisinghe, E. Stride, Release profile and characteristics of electrosprayed particles for oral delivery of a practically insoluble drug, J. R. Soc. Interface. 9 (2012) 2437–2449. https://doi.org/10.1098/rsif.2012.0166.

[8] X. Li, N. Anton, C. Arpagaus, F. Belleteix, T.F. Vandamme, Nanoparticles by spray drying using innovative new technology: The Büchi Nano Spray Dryer B-90, J. Control. Release. 147 (2010) 304–310. https://doi.org/10.1016/j.jconrel.2010.07.113.

[9] M. Cloupeau, B. Prunet-Foch, Electrostatic spraying of liquids in cone-jet mode, J. Electrostat. 22 (1989) 135–159. https://doi.org/10.1016/0304-3886(89)90081-8.

[10] G.M.H. Meesters, P.H.W. Vercoulen, J.C.M. Marijnissen, B. Scarlett, Generation of micron-sized droplets from the Taylor cone, J. Aerosol Sci. 23 (1992) 37–49. https://doi.org/10.1016/0021-8502(92)90316-N.

[11] J. Rosell-Llompart, J. Fernández de la Mora, Generation of monodisperse droplets 0.3 to 4 μm in diameter from electrified cone-jets of highly conducting and viscous liquids, J. Aerosol Sci. 25 (1994) 1093–1119. https://doi.org/10.1016/0021-8502(94)90204-6.

[12] S. V. Bhujbal, B. Mitra, U. Jain, Y. Gong, A. Agrawal, S. Karki, L.S. Taylor, S. Kumar, Q. (Tony) Zhou, Pharmaceutical amorphous solid dispersion: A review of manufacturing strategies, Acta Pharm. Sin. B. 11 (2021) 2505–2536. https://doi.org/10.1016/j.apsb.2021.05.014.

[13] D. Cun, C. Zhang, H. Bera, M. Yang, Particle engineering principles and technologies for pharmaceutical biologics, Adv. Drug Deliv. Rev. 174 (2021) 140–167. https://doi.org/10.1016/j.addr.2021.04.006.

[14] A. Ali, A. Zaman, E. Sayed, D. Evans, S. Morgan, C. Samwell, J. Hall, M.S. Arshad, N. Singh, O. Qutachi, M.-W. Chang, Z. Ahmad, Electrohydrodynamic atomisation driven design and engineering of opportunistic particulate systems for applications in drug delivery, therapeutics and pharmaceutics, Adv. Drug Deliv. Rev. 176 (2021) 113788. https://doi.org/10.1016/j.addr.2021.04.026.

[15] A. Jaworek, Electrostatic micro- and nanoencapsulation and electroemulsification: A brief review, J. Microencapsul. 25 (2008) 443–468. https://doi.org/10.1080/02652040802049109.

[16] E. Bodnár, J. Grifoll, J. Rosell-Llompart, Polymer solution electrospraying: A tool for engineering particles and films with controlled morphology, J. Aerosol Sci. 125 (2018) 93–118. https://doi.org/10.1016/j.jaerosci.2018.04.012.

[17] B. Almería, W. Deng, T.M. Fahmy, A. Gomez, Controlling the morphology of electrospray-generated PLGA microparticles for drug delivery, J. Colloid Interface Sci. 343 (2010) 125–133. https://doi.org/10.1016/j.jcis.2009.10.002.

[18] D.N. Nguyen, C. Clasen, G. Van den Mooter, Pharmaceutical applications of electrospraying, J. Pharm. Sci. 105 (2016) 2601–2620. https://doi.org/10.1016/j.xphs.2016.04.024.

[19] J. Xie, J. Jiang, P. Davoodi, M.P. Srinivasan, C.H. Wang, Electrohydrodynamic atomization: A two-decade effort to produce and process micro-/nanoparticulate materials, Chem. Eng. Sci. 125 (2015) 32–57. https://doi.org/10.1016/j.ces.2014.08.061.

[20] B.Y. Shekunov, P. Chattopadhyay, H.H.Y. Tong, A.H.L. Chow, Particle size analysis in pharmaceutics: Principles, methods and applications, Pharm. Res. 24 (2007) 203–227. https://doi.org/10.1007/s11095-006-9146-7.

[21] D.M. Webster, P. Sundaram, M.E. Byrne, Injectable nanomaterials for drug delivery: Carriers, targeting moieties, and therapeutics, Eur. J. Pharm. Biopharm. 84 (2013) 1–20. https://doi.org/10.1016/j.ejpb.2012.12.009.

[22] P. Jayaraman, C. Gandhimathi, J.R. Venugopal, D.L. Becker, S. Ramakrishna, D.K. Srinivasan, Controlled release of drugs in electrosprayed nanoparticles for bone tissue engineering, Adv. Drug Deliv. Rev. 94 (2015) 77–95. https://doi.org/10.1016/j.addr.2015.09.007.

[23] E.M. Kelder, J.C.M. Marijnissen, S.W. Karuga, EDHA for energy production, storage and conversion devices, J. Aerosol Sci. 125 (2018) 119–147. https://doi.org/10.1016/j.jaerosci.2018.04.011.

[24] J.L. Castillo, S. Martin, D. Rodriguez-Perez, F.J. Higuera, P.L. Garcia-Ybarra, Nanostructured porous coatings via electrospray atomization and deposition of nanoparticle suspensions, J. Aerosol Sci. 125 (2018) 148–163. https://doi.org/10.1016/j.jaerosci.2018.03.004.

[25] L.G. Gómez-Mascaraque, M. Hernández-Rojas, P. Tarancón, M. Tenon, N. Feuillère, J.F. Vélez Ruiz, S. Fiszman, A. López-Rubio, Impact of microencapsulation within electrosprayed proteins on the formulation of green tea extract-enriched biscuits, LWT - Food Sci. Technol. 81 (2017) 77–86. https://doi.org/10.1016/j.lwt.2017.03.041.

[26] M.D. Köse, Y. Başpınar, O. Bayraktar, Electroencapsulation (Electrospraying & Electrospinning) of Active Compounds for Food Applications, Curr. Pharm. Des. 25 (2019) 1881–1888. https://doi.org/10.2174/1381612825666190717125538.

[27] A.M. Gañán-Calvo, J.M. López-Herrera, M.A. Herrada, A. Ramos, J.M. Montanero, Review on the physics of electrospray: From electrokinetics to the operating conditions of single and coaxial Taylor cone-jets, and AC electrospray, J. Aerosol Sci. 125 (2018) 32–56. https://doi.org/10.1016/j.jaerosci.2018.05.002.

[28] N. Sochorakis, J. Grifoll, J. Rosell-Llompart, Scaling up of extractor-free electrosprays in linear arrays, Chem. Eng. Sci. 195 (2019) 281–298. https://doi.org/10.1016/j.ces.2018.09.006.

[29] R. Haj-Ahmad, M. Rasekh, K. Nazari, E. V. Onaiwu, B. Yousef, S. Morgan, D. Evans, M.-W. Chang, J. Hall, C. Samwell, Z. Ahmad, Stable increased formulation atomization using a multi-tip nozzle device, Drug Deliv. Transl. Res. 8 (2018) 1815–1827. https://doi.org/10.1007/s13346-018-0518-4.

[30] M. Parhizkar, P.J.T. Reardon, J.C. Knowles, R.J. Browning, E. Stride, R.B. Pedley, T. Grego, M. Edirisinghe, Performance of novel high throughput multi electrospray systems for forming of polymeric micro/nanoparticles, Mater. Des. 126 (2017) 73–84.

https://doi.org/10.1016/j.matdes.2017.04.029.

[31] B. Almería, T.M. Fahmy, A. Gomez, A multiplexed electrospray process for single-step synthesis of stabilized polymer particles for drug delivery, J. Control. Release. 154 (2011) 203–210. https://doi.org/10.1016/j.jconrel.2011.05.018.

[32] W. Deng, C.M. Waits, B. Morgan, A. Gomez, Compact multiplexing of monodisperse electrosprays, J. Aerosol Sci. 40 (2009) 907–918. https://doi.org/10.1016/j.jaerosci.2009.07.002.

[33] R. Bocanegra, D. Galán, M. Márquez, I.G. Loscertales, A. Barrero, Multiple electrosprays emitted from an array of holes, J. Aerosol Sci. 36 (2005) 1387–1399. https://doi.org/10.1016/j.jaerosci.2005.04.003.

[34] D. Olvera-Trejo, L.F. Velásquez-García, Additively manufactured MEMS multiplexed coaxial electrospray sources for high-throughput, uniform generation of core–shell microparticles, Lab Chip. 16 (2016) 4121–4132. https://doi.org/10.1039/C6LC00729E.

[35] C.J. Batty, M.D. Gallovic, J. Williams, T.M. Ross, E.M. Bachelder, K.M. Ainslie, Multiplexed electrospray enables high throughput production of cGAMP microparticles to serve as an adjuvant for a broadly acting influenza vaccine, Int. J. Pharm. 622 (2022) 121839. https://doi.org/https://doi.org/10.1016/j.ijpharm.2022.121839.

[36] A. Carrasco-Munoz, E. Barbero-Colmenar, E. Bodnár, J. Grifoll, J. Rosell-Llompart, Monodisperse droplets and particles by efficient neutralization of electrosprays, J. Aerosol Sci. 160 (2022) 105909. https://doi.org/10.1016/j.jaerosci.2021.105909.

[37] W.S. Mustika, D.A. Hapidin, C. Saputra, M.M. Munir, Dual needle corona discharge to generate stable bipolar ion for neutralizing electrosprayed nanoparticles, Adv. Powder Technol. 32 (2021) 166–174. https://doi.org/10.1016/j.apt.2020.11.026.

[38] Z.-C. Yao, C. Zhang, Z. Ahmad, Y. Peng, M.-W. Chang, Microparticle Formation via Tri-needle Coaxial Electrospray at Stable Jetting Modes, Ind. Eng. Chem. Res. 59 (2020) 14423–14432. https://doi.org/10.1021/acs.iecr.0c02677.

[39] C. Zhang, Y. Li, Y. Hu, Y. Peng, Z. Ahmad, J.-S. Li, M.-W. Chang, Porous Yolk–Shell Particle Engineering via Nonsolvent-Assisted Trineedle Coaxial Electrospraying for Burn-Related Wound Healing, ACS Appl. Mater. Interfaces. 11 (2019) 7823–7835. https://doi.org/10.1021/acsami.8b22112.

[40] I.G. Loscertales, A. Barrero, I. Guerrero, R. Cortijo, M. Marquez, A.M. Gañán-Calvo, Micro / nano encapsulation via electrified coaxial liquid jets, Science (80-.). 295 (2002) 1695–1698. https://doi.org/10.1126/science.1067595.

[41] Y.H. Lee, M.Y. Bai, D.R. Chen, Multidrug encapsulation by coaxial tri-capillary electrospray, Colloids Surfaces B Biointerfaces. 82 (2011) 104–110. https://doi.org/10.1016/j.colsurfb.2010.08.022.

[42] R.T. Steipel, M.D. Gallovic, C.J. Batty, E.M. Bachelder, K.M. Ainslie, Electrospray for generation of drug delivery and vaccine particles applied in vitro and in vivo, Mater. Sci. Eng. C. 105 (2019) 110070. https://doi.org/10.1016/j.msec.2019.110070.

[43] S.K. Boda, X. Li, J. Xie, Electrospraying an enabling technology for pharmaceutical and biomedical applications: A review, J. Aerosol Sci. 125 (2018) 164–181. https://doi.org/10.1016/j.jaerosci.2018.04.002.

[44] P. Mehta, R. Haj-Ahmad, M. Rasekh, M.S. Arshad, A. Smith, S.M. van der Merwe, X. Li, M.W. Chang, Z. Ahmad, Pharmaceutical and biomaterial engineering via electrohydrodynamic atomization technologies, Drug Discov. Today. 22 (2017) 157–165. https://doi.org/10.1016/j.drudis.2016.09.021.

[45] N. Bock, M.A. Woodruff, D.W. Hutmacher, T.R. Dargaville, Electrospraying, a reproducible method for production of polymeric microspheres for biomedical applications, Polymers

(Basel). 3 (2011) 131–149. https://doi.org/10.3390/polym3010131.

[46] A.J. Hijano, I.G. Loscertales, S.E. Ibáñez, F.J. Higuera, Periodic emission of droplets from an oscillating electrified meniscus of a low-viscosity, highly conductive liquid, Phys. Rev. E - Stat. Nonlinear, Soft Matter Phys. 91 (2015) 013011 (12pp). https://doi.org/10.1103/PhysRevE.91.013011.

[47] J. Rosell-Llompart, J. Grifoll, I.G. Loscertales, Electrosprays in the cone-jet mode: From Taylor cone formation to spray development, J. Aerosol Sci. 125 (2018) 2–31. https://doi.org/10.1016/j.jaerosci.2018.04.008.

[48] B. Almería, A. Gomez, Electrospray synthesis of monodisperse polymer particles in a broad (60 nm-2 μm) diameter range: Guiding principles and formulation recipes, J. Colloid Interface Sci. 417 (2014) 121–130. https://doi.org/10.1016/j.jcis.2013.11.037.

[49] R.P.A. Hartman, D.J. Brunner, D.M.A. Camelot, J.C.M. Marijnissen, B. Scarlett, Jet break-up in electrohydrodynamic atomization in the cone-jet mode, J. Aerosol Sci. 31 (2000) 65–95. https://doi.org/10.1016/S0021-8502(99)00034-8.

[50] G. Larsen, R. Spretz, R. Velarde-Ortiz, Use of coaxial gas jackets to stabilize Taylor cones of volatile solutions and to induce particle-to-fiber transitions, Adv. Mater. 16 (2004) 166–169. https://doi.org/10.1002/adma.200306021.

[51] E. Bodnár, J. Rosell-Llompart, Growth dynamics of granular films produced by electrospray, J. Colloid Interface Sci. 407 (2013) 536–545. https://doi.org/10.1016/j.jcis.2013.06.013.

[52] E. Bodnár, Electrospraying of polymer solutions for the generation of micro-particles, nanostructures, and granular films, Universitat Rovira i Virgili, 2016. http://www.tdx.cat/handle/10803/379820.

[53] P. Franco, I. De Marco, The Use of Poly(N-vinyl pyrrolidone) in the Delivery of Drugs: A Review, Polymers (Basel). 12 (2020) 1114. https://doi.org/https://doi.org/10.3390/polym12051114.

[54] A. Schittny, J. Huwyler, M. Puchkov, Mechanisms of increased bioavailability through amorphous solid dispersions: a review, Drug Deliv. 27 (2020) 110–127. https://doi.org/10.1080/10717544.2019.1704940.

[55] P. Tran, Y.C. Pyo, D.H. Kim, S.E. Lee, J.K. Kim, J.S. Park, Overview of the manufacturing methods of solid dispersion technology for improving the solubility of poorly water-soluble drugs and application to anticancer drugs, Pharmaceutics. 11 (2019) 1–26. https://doi.org/10.3390/pharmaceutics11030132.

[56] M. Guastaferro, L. Baldino, S. Cardea, E. Reverchon, Supercritical assisted electrospray/spinning to produce PVP+quercetin microparticles and microfibers, J. Taiwan Inst. Chem. Eng. 117 (2020) 278–286. https://doi.org/https://doi.org/10.1016/j.jtice.2020.12.017.

[57] Y.A. Rezeki, D.A. Hapidin, H. Rachmawati, M.M. Munir, K. Khairurrijal, Formation of electrosprayed composite nanoparticles from polyvinylpyrrolidone/mangosteen pericarp extract, Adv. Powder Technol. 31 (2020) 1811–1824. https://doi.org/10.1016/j.apt.2020.02.016.

[58] L.F. Chen, P.Y. Xu, C.P. Fu, R.K. Kankala, A.Z. Chen, S. Bin Wang, Fabrication of supercritical antisolvent (SAS) process-assisted fisetin-encapsulated poly (vinyl pyrrolidone) (PVP) nanocomposites for improved anticancer therapy, Nanomaterials. 10 (2020). https://doi.org/10.3390/nano10020322.

[59] E. Browne, R. Charifou, Z.A. Worku, R.P. Babu, A.M. Healy, Amorphous solid dispersions of ketoprofen and poly-vinyl polymers prepared via electrospraying and spray drying: A comparison of particle characteristics and performance, Int. J. Pharm. 566 (2019) 173–184. https://doi.org/10.1016/j.ijpharm.2019.05.062.

[60] A. Smeets, R. Koekoekx, C. Clasen, G. Van den Mooter, Amorphous solid dispersions of darunavir: Comparison between spray drying and electrospraying, Eur. J. Pharm. Biopharm. 130 (2018) 96–107. https://doi.org/10.1016/j.ejpb.2018.06.021.

[61] W. Kim, J.S. Kim, H.-G. Choi, S.G. Jin, C.-W. Cho, Novel ezetimibe-loaded fibrous microparticles for enhanced solubility and oral bioavailability by electrospray technique, J. Drug Deliv. Sci. Technol. 66 (2021). https://doi.org/10.1016/j.jddst.2021.102877.

[62] A.M. Yousaf, O. Mustapha, D.W. Kim, D.S. Kim, K.S. Kim, S.G. Jin, C.S. Yong, Y.S. Youn, Y.K. Oh, J.O. Kim, H.G. Choi, Novel electrosprayed nanospherules for enhanced aqueous solubility and oral bioavailability of poorly water-soluble fenofibrate, Int. J. Nanomedicine. 11 (2016) 213–221. https://doi.org/10.2147/IJN.S97496.

[63] F. Sadeghi, M. Ashofteh, A. Homayouni, M. Abbaspour, A. Nokhodchi, H.A. Garekani, Antisolvent precipitation technique: A very promising approach to crystallize curcumin in presence of polyvinyl pyrrolidon for solubility and dissolution enhancement, Colloids Surfaces B Biointerfaces. 147 (2016) 258–264. https://doi.org/10.1016/j.colsurfb.2016.08.004.

[64] R. Ali, P. Mehta, P. Kyriaki Monou, M.S. Arshad, E. Panteris, M. Rasekh, N. Singh, O. Qutachi, P. Wilson, D. Tzetzis, M.-W. Chang, D.G. Fatouros, Z. Ahmad, Electrospinning/electrospraying coatings for metal microneedles: A design of experiments (DOE) and quality by design (QbD) approach, Eur. J. Pharm. Biopharm. 156 (2020) 20–39. https://doi.org/https://doi.org/10.1016/j.ejpb.2020.08.023.

[65] M. Rasekh, C. Karavasili, Y.L. Soong, N. Bouropoulos, M. Morris, D. Armitage, X. Li, D.G. Fatouros, Z. Ahmad, Electrospun PVP–indomethacin constituents for transdermal dressings and drug delivery devices, Int. J. Pharm. 473 (2014) 95–104. https://doi.org/https://doi.org/10.1016/j.ijpharm.2014.06.059.

[66] L.S. Usmanova, M.A. Ziganshin, I.T. Rakipov, N.M. Lyadov, A.E. Klimovitskii, T.A. Mukhametzyanov, A. V. Gerasimov, Microspherical Particles of Solid Dispersion of Polyvinylpyrrolidone K29-32 for Inhalation Administration, Biomed Res. Int. 2018 (2018). https://doi.org/10.1155/2018/2412156.

[67] F. Kurniawansyah, R. Mammucari, N.R. Foster, Inhalable curcumin formulations by supercritical technology, Powder Technol. 284 (2015) 289–298. https://doi.org/10.1016/j.powtec.2015.04.083.

[68] P. Mehta, L. Justo, S. Walsh, M.S. Arshad, C.G. Wilson, C.K. O'Sullivan, S.M. Moghimi, I.S. Vizirianakis, K. Avgoustakis, D.G. Fatouros, Z. Ahmad, New platforms for multi-functional ocular lenses: Engineering double-sided functionalized nano-coatings, J. Drug Target. 23 (2015) 305–310. https://doi.org/10.3109/1061186X.2014.1001395.

[69] S. Toden, A. Goel, The Holy Grail of Curcumin and its Efficacy in Various Diseases: Is Bioavailability Truly a Big Concern?, Physiol. Behav. 176 (2018) 139–148. https://doi.org/10.1016/j.physbeh.2017.03.040.

[70] M. Gera, N. Sharma, M. Ghosh, D. Luong Huynh, S.J. Lee, T. Min, T. Kwon, D.K. Jeong, D.L. Huynh, S.J. Lee, T. Min, T. Kwon, D.K. Jeong, Nanoformulations of curcumin: an emerging paradigm for improved remedial application, Oncotarget. 8 (2017) 66680–66698. https://doi.org/10.18632/oncotarget.19164.

[71] M.M. Yallapu, M. Jaggi, S.C. Chauhan, Curcumin nanoformulations: a future nanomedicine for cancer, Drug Discov. Today. 17 (2012) 71–80. https://doi.org/https://doi.org/10.1016/j.drudis.2011.09.009.

[72] R.K. Maheshwari, A.K. Singh, J. Gaddipati, R.C. Srimal, Multiple biological activities of curcumin: A short review, Life Sci. 78 (2006) 2081–2087. https://doi.org/10.1016/j.lfs.2005.12.007.

[73] R. Adami, A. Di Capua, E. Reverchon, Supercritical Assisted Atomization for the production

of curcumin-biopolymer microspheres, Powder Technol. 305 (2017) 455–461. https://doi.org/10.1016/J.POWTEC.2016.10.020.

[74] S. Nogami, K. Minoura, N. Kiminami, Y. Kitaura, H. Uchiyama, K. Kadota, Y. Tozuka, Stabilizing effect of the cyclodextrins additive to spray-dried particles of curcumin/polyvinylpyrrolidone on the supersaturated state of curcumin, Adv. Powder Technol. 32 (2021) 1750–1756. https://doi.org/https://doi.org/10.1016/j.apt.2021.03.032.

[75] T. Thongnopkoon, C. Chittasupho, Curcumin composite particles prepared by spray drying and in vitro anti-cancer activity on lung cancer cell line, J. Drug Deliv. Sci. Technol. 45 (2018) 397–407. https://doi.org/10.1016/j.jddst.2018.04.006.

[76] D. Mustikasari, Y.A. Rezeki, M.M. Munir, H. Rachmawati, K. Khairurrijal, Turmeric extract-loaded polyvinylpyrrolidone spherical submicron particles produced using electrohydrodynamic atomization: Their physico-chemical properties and antioxidant activity, Mater. Res. Express. 6 (2019) 085415. https://doi.org/10.1088/2053-1591/ab272a.

[77] K. Chhouk, W. Diono, H. Kanda, M. Goto, Micronization for Enhancement of Curcumin Dissolution via Electrospraying Technique, ChemEngineering. 2 (2018) 11. https://doi.org/10.3390/chemengineering2040060.

[78] A.M. Gañán-Calvo, N. Rebollo-Muñoz, J.M. Montanero, The minimum or natural rate of flow and droplet size ejected by Taylor cone-jets: physical symmetries and scaling laws, New J. Phys. 15 (2013) 033035 (13pp). https://doi.org/10.1088/1367-2630/15/3/033035.

[79] C.J. Hogan, K.M. Yun, D.R. Chen, I.W. Lenggoro, P. Biswas, K. Okuyama, Controlled size polymer particle production via electrohydrodynamic atomization, Colloids Surfaces A Physicochem. Eng. Asp. 311 (2007) 67–76. https://doi.org/10.1016/j.colsurfa.2007.05.072.

[80] S. Verdoold, L.L.F. Agostinho, C.U. Yurteri, J.C.M. Marijnissen, A generic electrospray classification, J. Aerosol Sci. 67 (2014) 87–103. https://doi.org/10.1016/j.jaerosci.2013.09.008.

[81] A. Suhendi, M.M. Munir, A.B. Suryamas, A.B.D. Nandiyanto, T. Ogi, K. Okuyama, Control of cone-jet geometry during electrospray by an electric current, Adv. Powder Technol. 24 (2013) 532–536. https://doi.org/https://doi.org/10.1016/j.apt.2012.10.009.

[82] J.M. López-Herrera, A.M. Gañán-Calvo, A note on charged capillary jet breakup of conducting liquids: experimental validation of a viscous one-dimensional model, J. Fluid Mech. 501 (2004) 303–326. https://doi.org/10.1017/S0022112003007560.

[83] G. Taylor, Disintegration of water drops in an electric field, Proc. R. Soc. A Math. Phys. Eng. Sci. 280 (1964) 383–397. https://doi.org/10.1098/rspa.1964.0151.

[84] D.A. Saville, Electrohydrodynamics: The Taylor-Melcher leaky dielectric model, Annu. Rev. Fluid Mech. 29 (1997) 27–64. https://doi.org/10.1146/annurev.fluid.29.1.27.

[85] D. Duft, T. Achtzehn, R. Müller, B. a Huber, T. Leisner, Coulomb fission: Rayleigh jets from levitated microdroplets., Nature. 421 (2003) 128. https://doi.org/10.1038/421128a.

[86] R.L. Grimm, J.L. Beauchamp, Dynamics of field-induced droplet ionization: Time-resolved studies of distortion, jetting, and progeny formation from charged and neutral methanol droplets exposed to strong electric fields, J. Phys. Chem. B. 109 (2005) 8244–8250. https://doi.org/10.1021/jp0450540.

[87] D. Li, M. Marquez, Y. Xia, Capturing electrified nanodroplets under Rayleigh instability by coupling electrospray with a sol-gel reaction, Chem. Phys. Lett. 445 (2007) 271–275. https://doi.org/10.1016/j.cplett.2007.07.090.

[88] M. Guettari, A. Belaidi, S. Abel, T. Tajouri, Polyvinylpyrrolidone Behavior in Water/Ethanol Mixed Solvents: Comparison of Modeling Predictions with Experimental Results, J. Solution Chem. 46 (2017) 1404–1417. https://doi.org/10.1007/s10953-017-0649-0.

[89] R.L. Matos, T. Lu, V. Prosapio, C. McConville, G. Leeke, A. Ingram, Coprecipitation of curcumin/PVP with enhanced dissolution properties by the supercritical antisolvent process, J. CO2 Util. 30 (2019) 48–62. https://doi.org/10.1016/j.jcou.2019.01.005.

[90] A. Smeets, R. Koekoekx, W. Ruelens, M. Smet, C. Clasen, G. Van den Mooter, Gastro-resistant encapsulation of amorphous solid dispersions containing darunavir by coaxial electrospraying, Int. J. Pharm. (2019) 118885. https://doi.org/10.1016/j.ijpharm.2019.118885.

[91] J. Xie, L.K. Lim, Y. Phua, J. Hua, C.H. Wang, Electrohydrodynamic atomization for biodegradable polymeric particle production, J. Colloid Interface Sci. 302 (2006) 103–112. https://doi.org/10.1016/j.jcis.2006.06.037.

[92] C.H. Park, J. Lee, Electrosprayed polymer particles: Effect of the solvent properties, J. Appl. Polym. Sci. 114 (2009) 430–437. https://doi.org/10.1002/app.30498.

[93] J. Yao, L. Kuang Lim, J. Xie, J. Hua, C.H. Wang, Characterization of electrospraying process for polymeric particle fabrication, J. Aerosol Sci. 39 (2008) 987–1002. https://doi.org/10.1016/j.jaerosci.2008.07.003.

[94] M.A. Boraey, R. Vehring, Diffusion controlled formation of microparticles, J. Aerosol Sci. 67 (2014) 131–143. https://doi.org/10.1016/j.jaerosci.2013.10.002.

[95] A.B.D. Nandiyanto, K. Okuyama, Progress in developing spray-drying methods for the production of controlled morphology particles: From the nanometer to submicrometer size ranges, Adv. Powder Technol. 22 (2011) 1–19. https://doi.org/10.1016/j.apt.2010.09.011.

[96] A. Paradkar, A.A. Ambike, B.K. Jadhav, K.R. Mahadik, Characterization of curcumin-PVP solid dispersion obtained by spray drying, Int. J. Pharm. 271 (2004) 281–286. https://doi.org/10.1016/j.ijpharm.2003.11.014.

[97] N. Kaewnopparat, S. Kaewnopparat, A. Jangwang, D. Maneenaun, T. Chuchome, P. Panichayupakaranant, Increased solubility, dissolution and physicochemical studies of curcumin-polyvinylpyrrolidone K-30 solid dispersions, World Acad. Sci. Eng. Technol. 31 (2009) 225–230.

[98] J. Fernández de la Mora, I.G. Loscertales, The current emitted by highly conducting Taylor cones, J. Fluid Mech. 260 (1994) 155–184. https://doi.org/10.1017/S0022112094003472.

[99] J.J. Jasper, The Surface Tension of Pure Liquid Compounds, J. Phys. Chem. Ref. Data. 1 (1972) 841–1010. https://doi.org/10.1063/1.3253106.

[100] P.R.K. Mohan, G. Sreelakshmi, C. V Muraleedharan, R. Joseph, Water soluble complexes of curcumin with cyclodextrins: Characterization by FT-Raman spectroscopy, Vib. Spectrosc. 62 (2012) 77–84. https://doi.org/https://doi.org/10.1016/j.vibspec.2012.05.002.

[101] P. Tsekova, M. Spasova, N. Manolova, I. Rashkov, N. Markova, A. Georgieva, R. Toshkova, Electrospun cellulose acetate membranes decorated with curcumin-PVP particles: preparation, antibacterial and antitumor activities, J. Mater. Sci. Mater. Med. 29 (2018) 9. https://doi.org/10.1007/s10856-017-6014-4.

[102] Z. Mai, J. Chen, T. He, Y. Hu, X. Dong, H. Zhang, W. Huang, F. Ko, W. Zhou, Electrospray biodegradable microcapsules loaded with curcumin for drug delivery systems with high bioactivity, RSC Adv. 7 (2017) 1724–1734. https://doi.org/10.1039/c6ra25314h.

[103] R. Paranthaman, J.A. Moses, C. Anandharamakrishnan, Powder X-ray diffraction conditions for screening curcumin in turmeric powder, J. Food Meas. Charact. 16 (2022) 1105–1113. https://doi.org/10.1007/s11694-021-01225-w.

[104] L.A. Wegiel, Y. Zhao, L.J. Mauer, K.J. Edgar, L.S. Taylor, Curcumin amorphous solid dispersions: the influence of intra and intermolecular bonding on physical stability, Pharm. Dev. Technol. 19 (2014) 976–986. https://doi.org/10.3109/10837450.2013.846374.

[105] E.M. Abdelrazek, A.M. Abdelghany, S.I. Badr, M.A. Morsi, Structural, optical,

morphological and thermal properties of PEO/PVP blend containing different concentrations of biosynthesized Au nanoparticles, J. Mater. Res. Technol. 7 (2018) 419–431. https://doi.org/https://doi.org/10.1016/j.jmrt.2017.06.009.

[106] X. Li, M.A. Kanjwal, L. Lin, I.S. Chronakis, Electrospun polyvinyl-alcohol nanofibers as oral fast-dissolving delivery system of caffeine and riboflavin, Colloids Surfaces B Biointerfaces. 103 (2013) 182–188. https://doi.org/https://doi.org/10.1016/j.colsurfb.2012.10.016.

Table 1. Compositions and properties of the curcumin (CUR) - polyvinylpyrrolidone (PVP) solutions, experimental conditions (flow rate) and predicted and measured data. (RH < 5%.)

Solution code	[CUR] (%w/w)	[PVP] (%w/w)	CUR weight ratio (%)	Electrical conductivity k (µS/cm)	Density[a] ρ (kg/m^3)	Predicted minimum flow rate[b] Q_{min} (µL/min)	Solution flow rate Q (µL/min)	Predicted current[c] I (nA)	Average current I_{exp} (nA)	Predicted droplet diameter[d] d_D (µm)	Particle size mean[e] d_P (µm) ±SD
Solvent system: ethanol											
0.1C-1P	0.1	1	9.1	4.6 (22.6 ºC)	794	0.80	0.75	29	20	1.05	0.499 ± 0.049
0.1C-3P	0.1	3	3.2	8.8 (19.9 ºC)	803	0.41	0.75	41	30	0.94	0.521 ± 0.047
							1.5	58	43	1.33	0.674 ± 0.056
							3	82	70	1.88	0.852 ± 0.068
0.1C-5P	0.1	5	2.0	13.1 (21.6 ºC)	808	0.27	1.5	70	60	1.25	0.847 ± 0.070
0.1C-8P	0.1	8	1.2	18.2 (22.0 ºC)	817	0.19	1.5	83	67	1.19	0.900 ± 0.091
0.1C-10P	0.1	10	1.0	19.8 (21.9 ºC)	823	0.18	1	71	45	0.96	0.803 ± 0.071
Solvent system: ethanol/acetone (1:1 v/v)											
0C-5P	0	5	0	18.3 (22.4 ºC)	814	0.20	0.75	62	42	0.82	0.472 ± 0.049
1C-5P	1	5	16.7	14.6 (24.0 ºC)	815	0.25	0.75	55	35	0.85	0.497 ± 0.053
2.5C-5P	2.5	5	33.3	12.1 (23.7 ºC)	818	0.30	0.75	50	30	0.88	0.693 ± 0.059
5C-0P	5	0	100	3.24 (21.8 ºC)	810	1.13	0.75	26	20	1.10	0.435 ± 0.066
5C-1P	5	1	83.3	4.9 (22.2 ºC)	815	0.74	0.75	32	25	1.02	0.564 ± 0.043
5C-2.5P	5	2.5	66.7	9.7 (21.4 ºC)	818	0.37	0.75	45	30	0.92	0.690 ± 0.081
5C-5P	5	5	50	12.1 (24.0 ºC)	820	0.30	0.75	50	35	0.88	0.747 ± 0.067
7.5C-5P	7.5	5	60	11.6 (25.3 ºC)	818	0.31	1.5	70	45	1.26	1.06 ± 0.11

[a] Estimated values for 2.5C-5P, 5C-2.5P, 5C-1P and 7.5C-5P (more details in the Supplementary Information file, SI.1.).

[b] $Q_{min} = Q_0\beta$ (1); $Q_0 = \frac{\sigma\varepsilon_0}{\rho k}$ (2) [78]

[c,d] $\frac{d_D}{d_0} = \left(\frac{Q}{Q_0}\right)^{0.5}$ (4); $\frac{I}{I_0} = 2.6\left(\frac{Q}{Q_0}\right)^{0.5}$ (5), where $d_0 = \left(\frac{\sigma\varepsilon_0^2}{\rho k^2}\right)^{\frac{1}{3}}$ (6); and $I_0 = \sigma\left(\frac{\varepsilon_0}{\rho}\right)^{0.5}$ (7), [27]

[e] d_P is either the Feret diameter (d_F) or the projected area-equivalent diameter (d_S), as explained in Section 2.3. SD = standard deviation

Figure 01

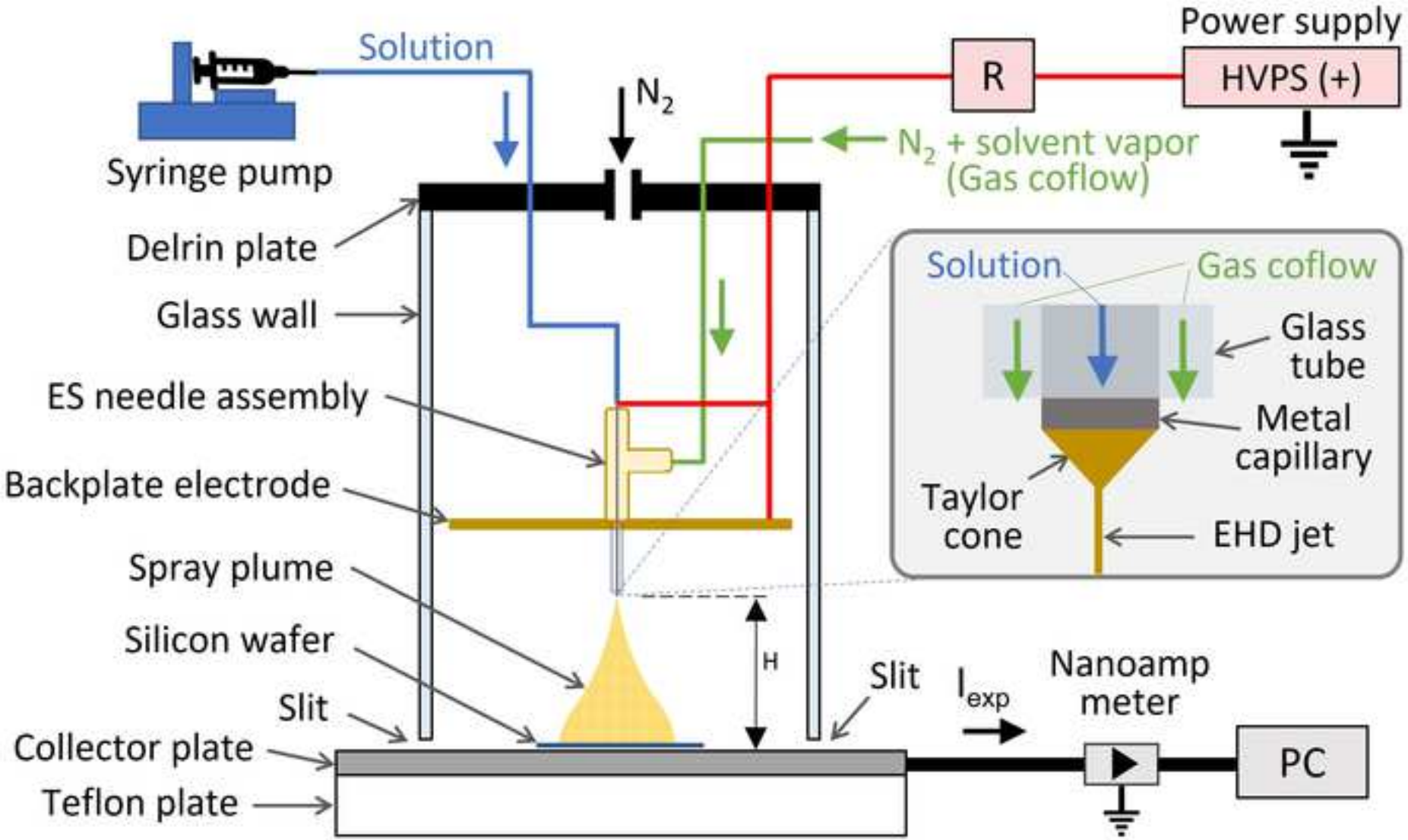
Solution
Syringe pump
N_2
R
Power supply
HVPS (+)
N_2 + solvent vapor
(Gas coflow)
Delrin plate
Glass wall
ES needle assembly
Backplate electrode
Spray plume
Silicon wafer
Slit
Collector plate
Teflon plate
H
Slit
I_{exp}
Nanoamp meter
PC
Solution
Gas coflow
Glass tube
Metal capillary
Taylor cone
EHD jet

Figure 02

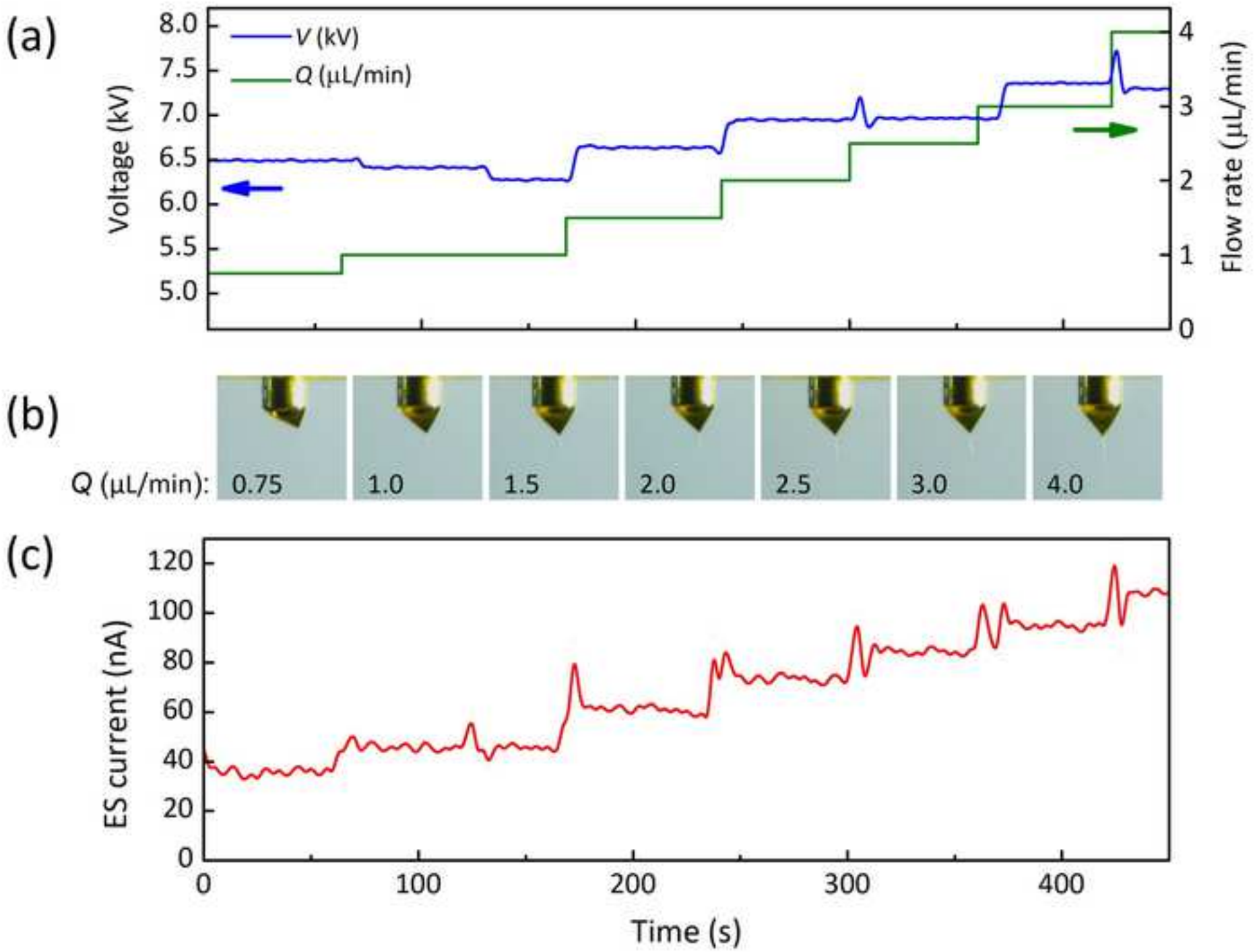
(a)
V (kV)
Q (μL/min)
Voltage (kV)
Flow rate (μL/min)
8.0
7.5
7.0
6.5
6.0
5.5
5.0
4
3
2
1
0
(b)
Q (μL/min):
0.75
1.0
1.5
2.0
2.5
3.0
4.0
(c)
ES current (nA)
120
100
80
60
40
20
0
0
100
200
300
400
Time (s)

Figure 03

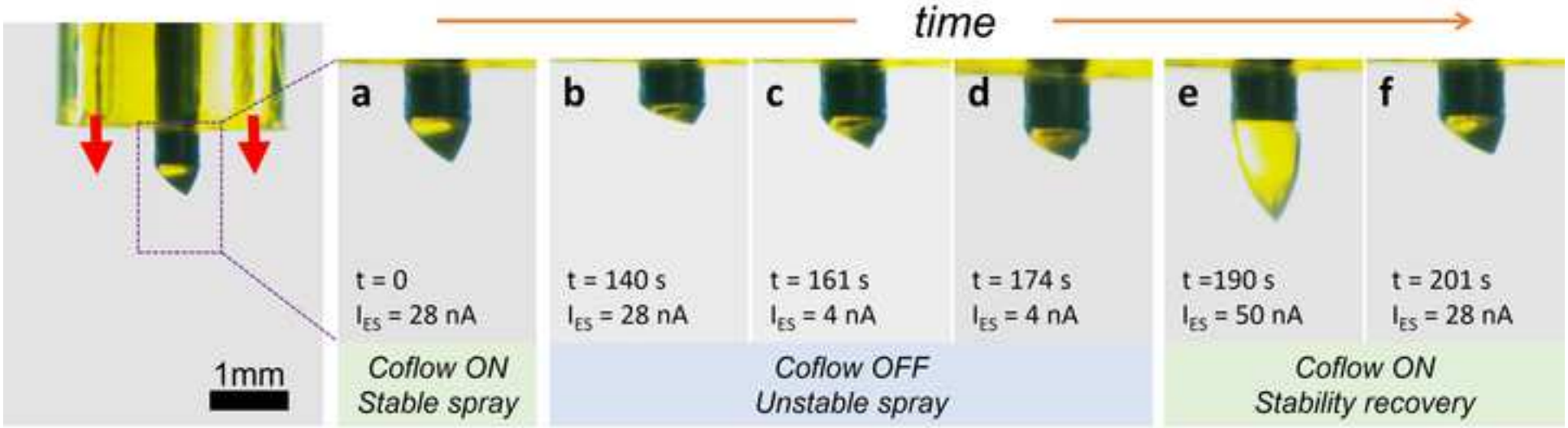
time
a
b
c
d
e
f
t = 0
I_ES = 28 nA
t = 140 s
I_ES = 28 nA
t = 161 s
I_ES = 4 nA
t = 174 s
I_ES = 4 nA
t =190 s
I_ES = 50 nA
t = 201 s
I_ES = 28 nA
1mm
Coflow ON
Stable spray
Coflow OFF
Unstable spray
Coflow ON
Stability recovery

Figure 04

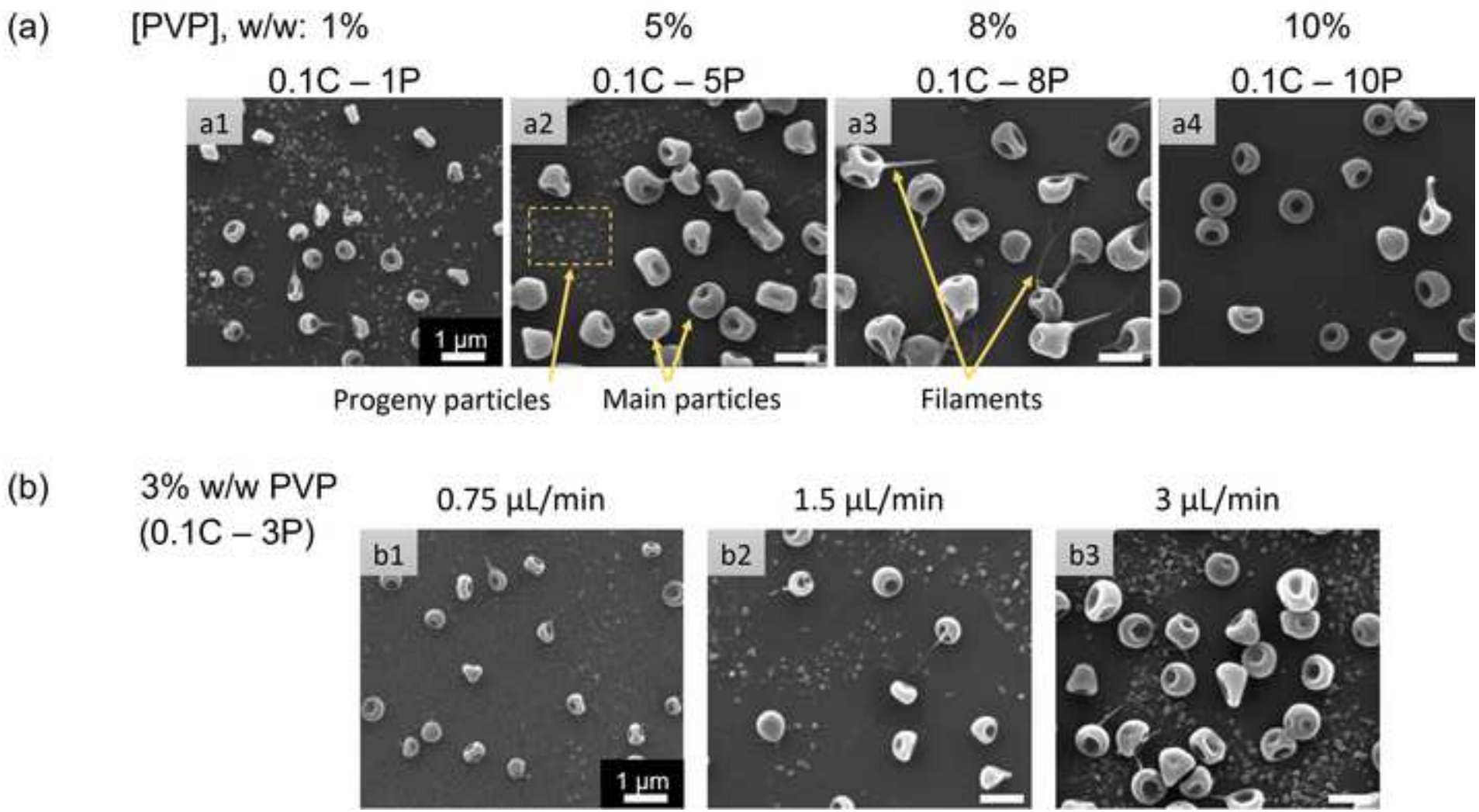
(a)
[PVP], w/w: 1%
5%
8%
10%
0.1C – 1P
0.1C – 5P
0.1C – 8P
0.1C – 10P
a1
a2
a3
a4
1 µm
Progeny particles
Main particles
Filaments
(b)
3% w/w PVP
(0.1C – 3P)
0.75 µL/min
1.5 µL/min
3 µL/min
b1
b2
b3
1 µm

Figure 05

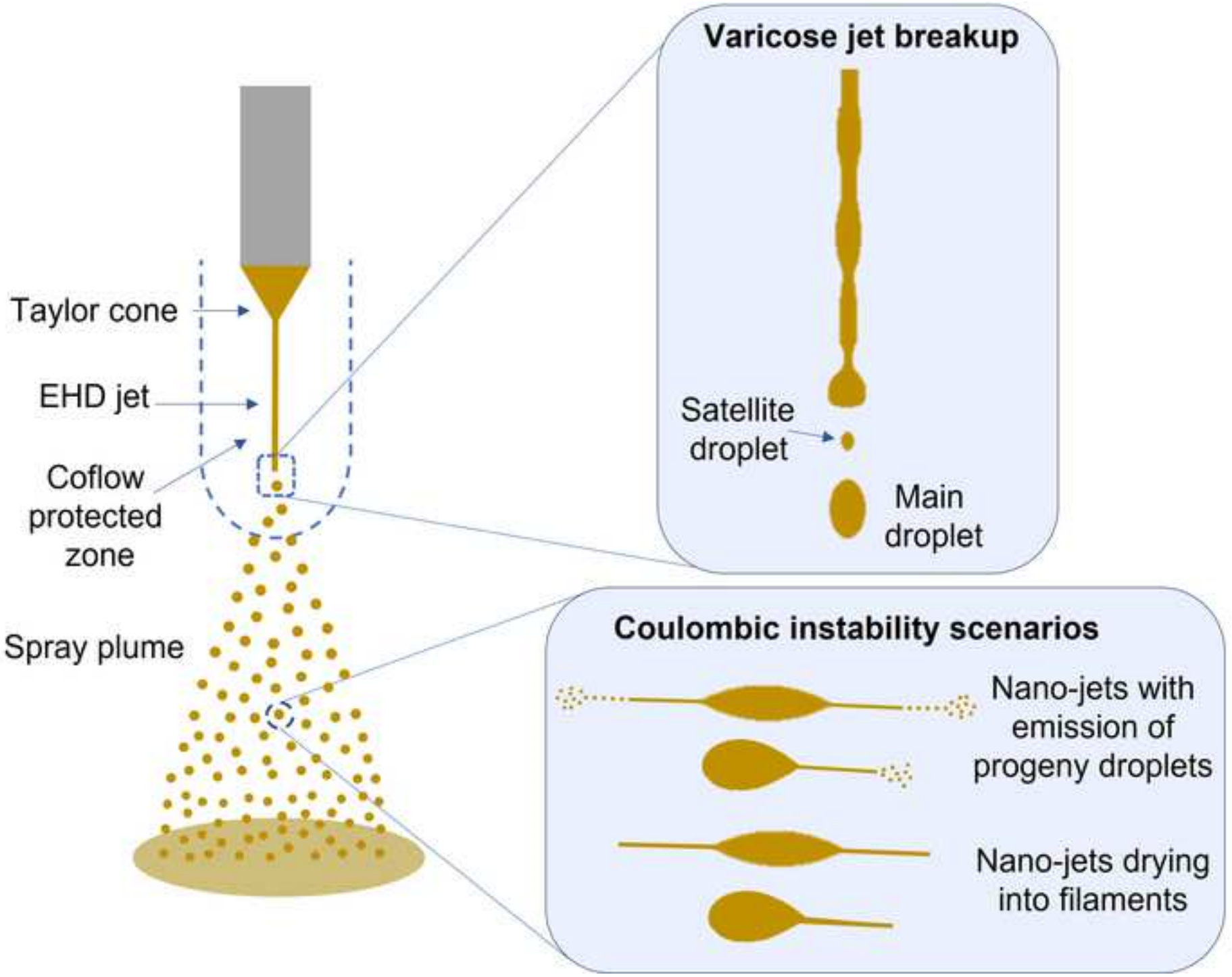
Varicose jet breakup
Satellite droplet
Main droplet
Taylor cone
EHD jet
Coflow protected zone
Spray plume
Coulombic instability scenarios
Nano-jets with emission of progeny droplets
Nano-jets drying into filaments

Figure 06

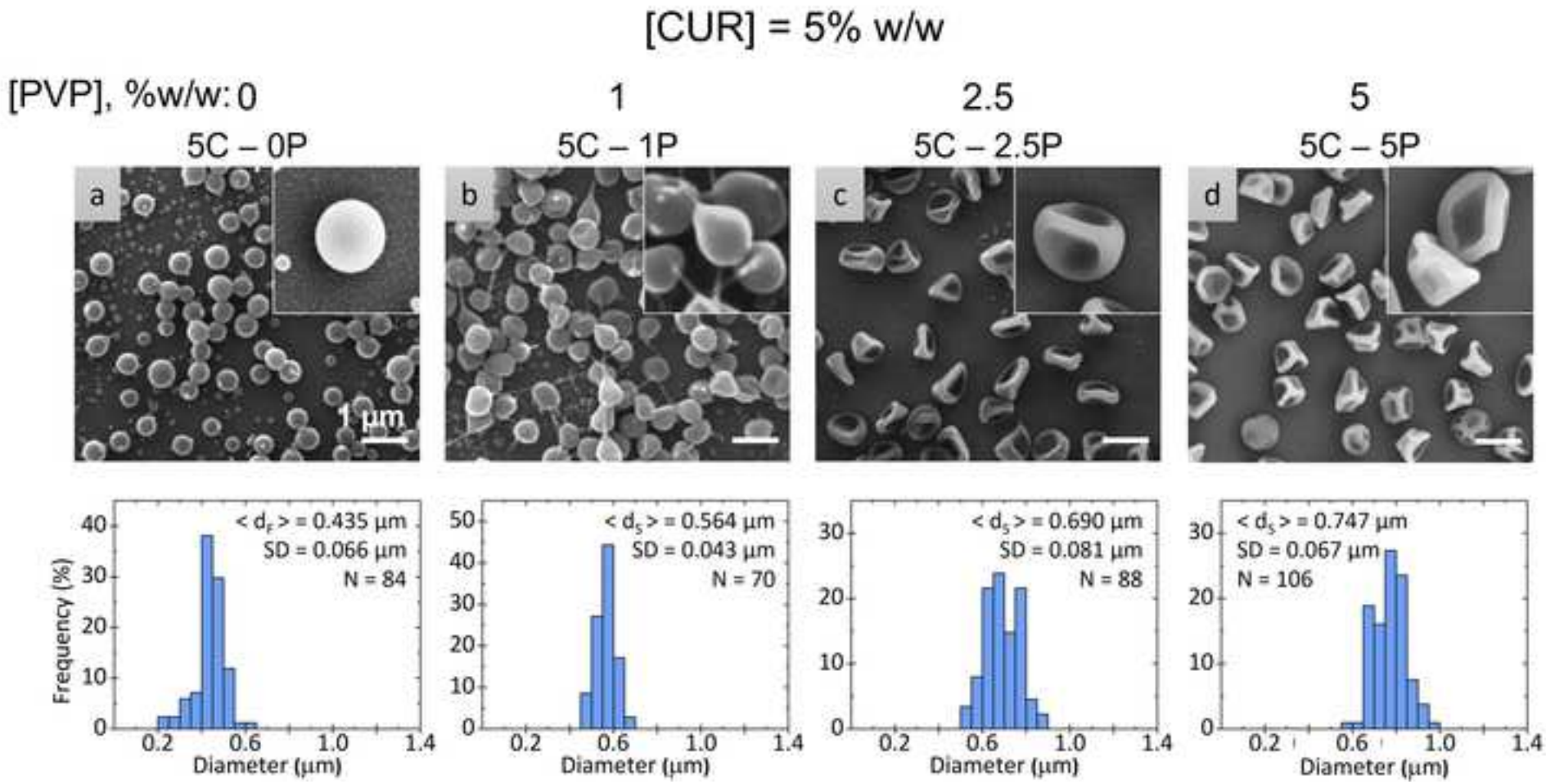
[CUR] = 5% w/w
[PVP], %w/w: 0
1
2.5
5
5C – 0P
5C – 1P
5C – 2.5P
5C – 5P
a
b
c
d
1 µm
< d_F > = 0.435 µm
SD = 0.066 µm
N = 84
< d_S > = 0.564 µm
SD = 0.043 µm
N = 70
< d_S > = 0.690 µm
SD = 0.081 µm
N = 88
< d_S > = 0.747 µm
SD = 0.067 µm
N = 106
Frequency (%)
Diameter (µm)

Figure 07

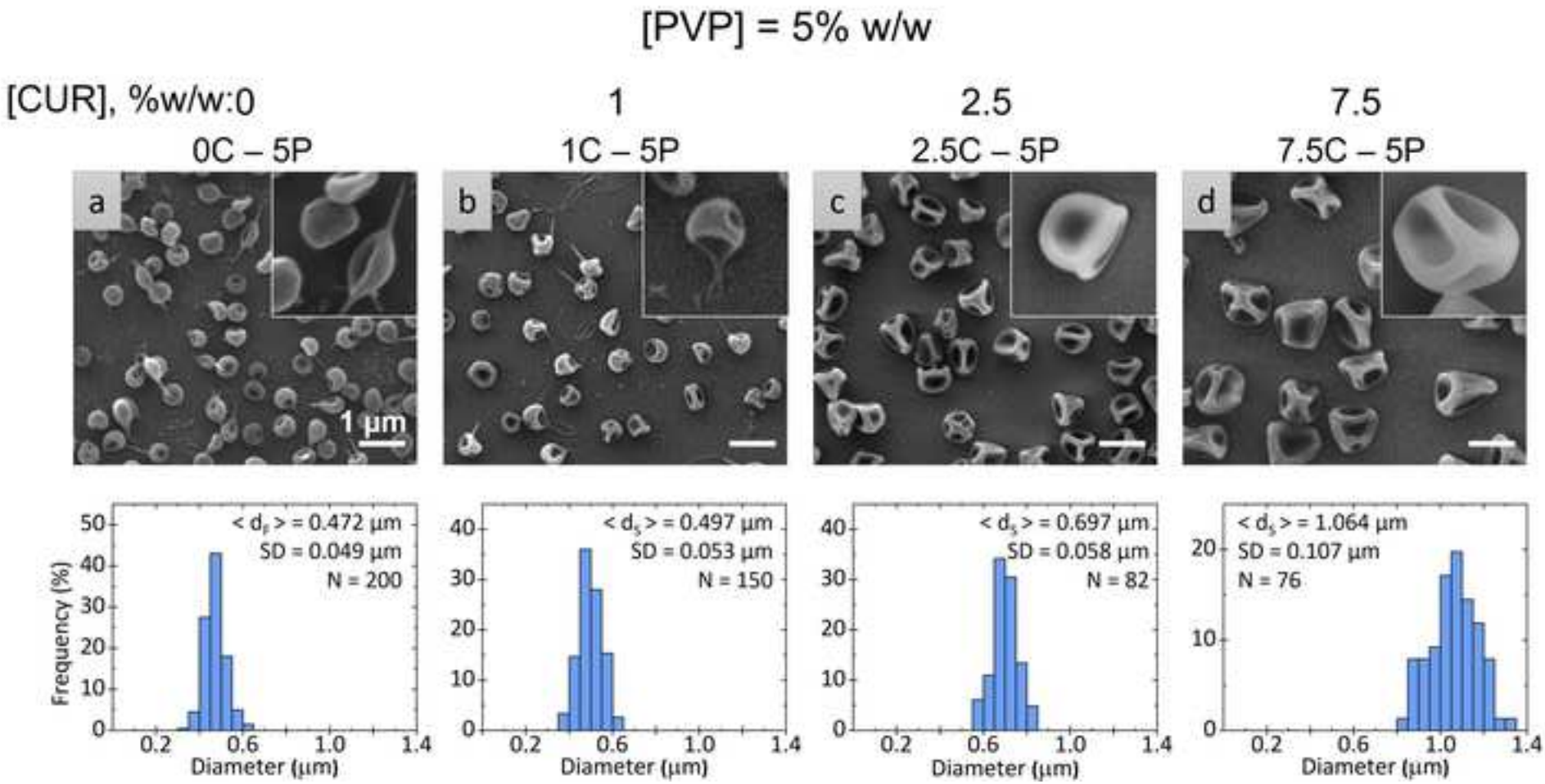
[PVP] = 5% w/w
[CUR], %w/w:0
1
2.5
7.5
0C – 5P
1C – 5P
2.5C – 5P
7.5C – 5P
a
b
c
d
1 µm
Frequency (%)
< d_f > = 0.472 µm
SD = 0.049 µm
N = 200
< d_f > = 0.497 µm
SD = 0.053 µm
N = 150
< d_f > = 0.697 µm
SD = 0.058 µm
N = 82
< d_f > = 1.064 µm
SD = 0.107 µm
N = 76
Diameter (µm)

Figure 08

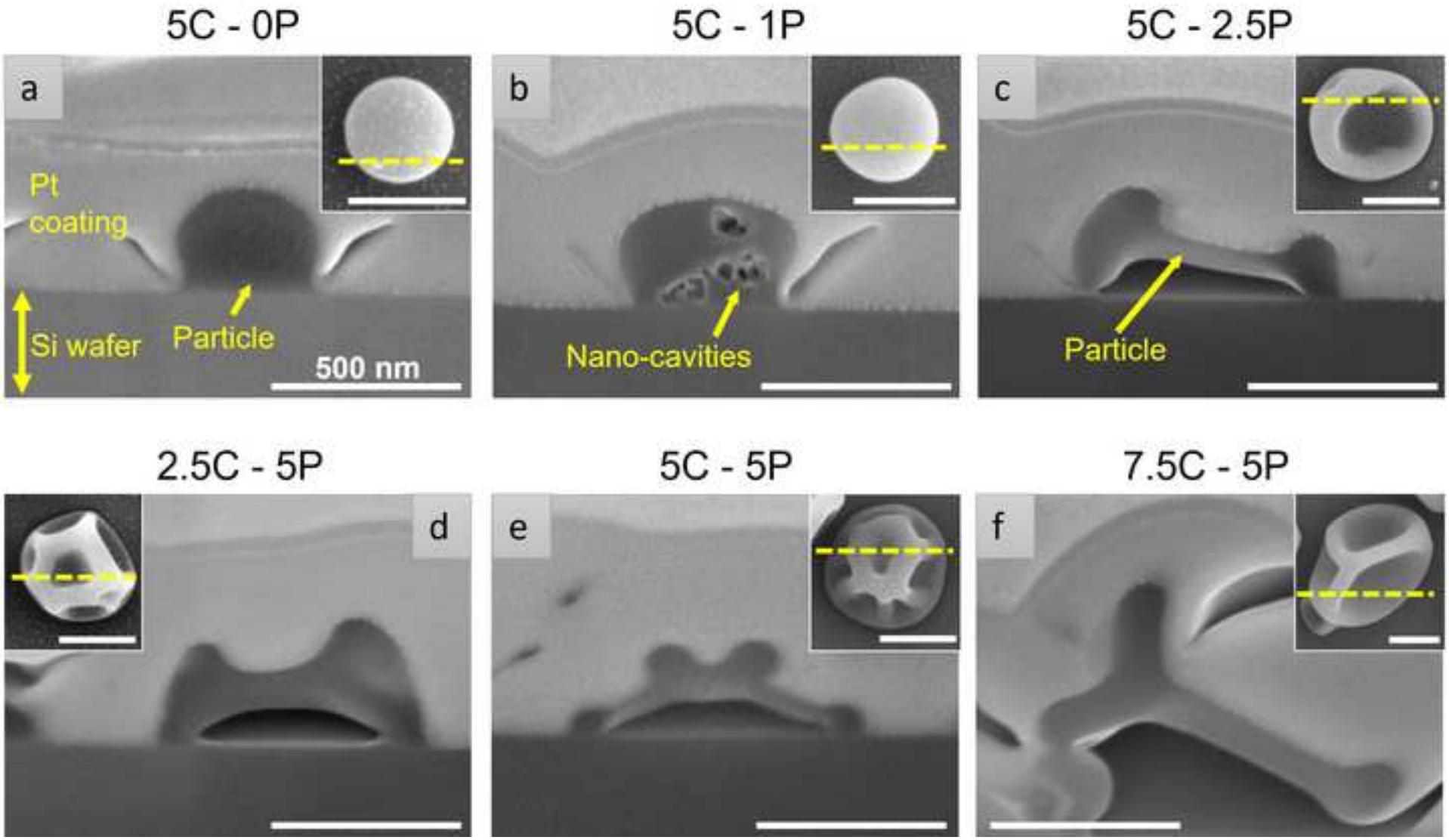
5C - 0P
5C - 1P
5C - 2.5P
a
b
c
Pt coating
Si wafer
Particle
500 nm
Nano-cavities
Particle
2.5C - 5P
5C - 5P
7.5C - 5P
d
e
f

Figure 09

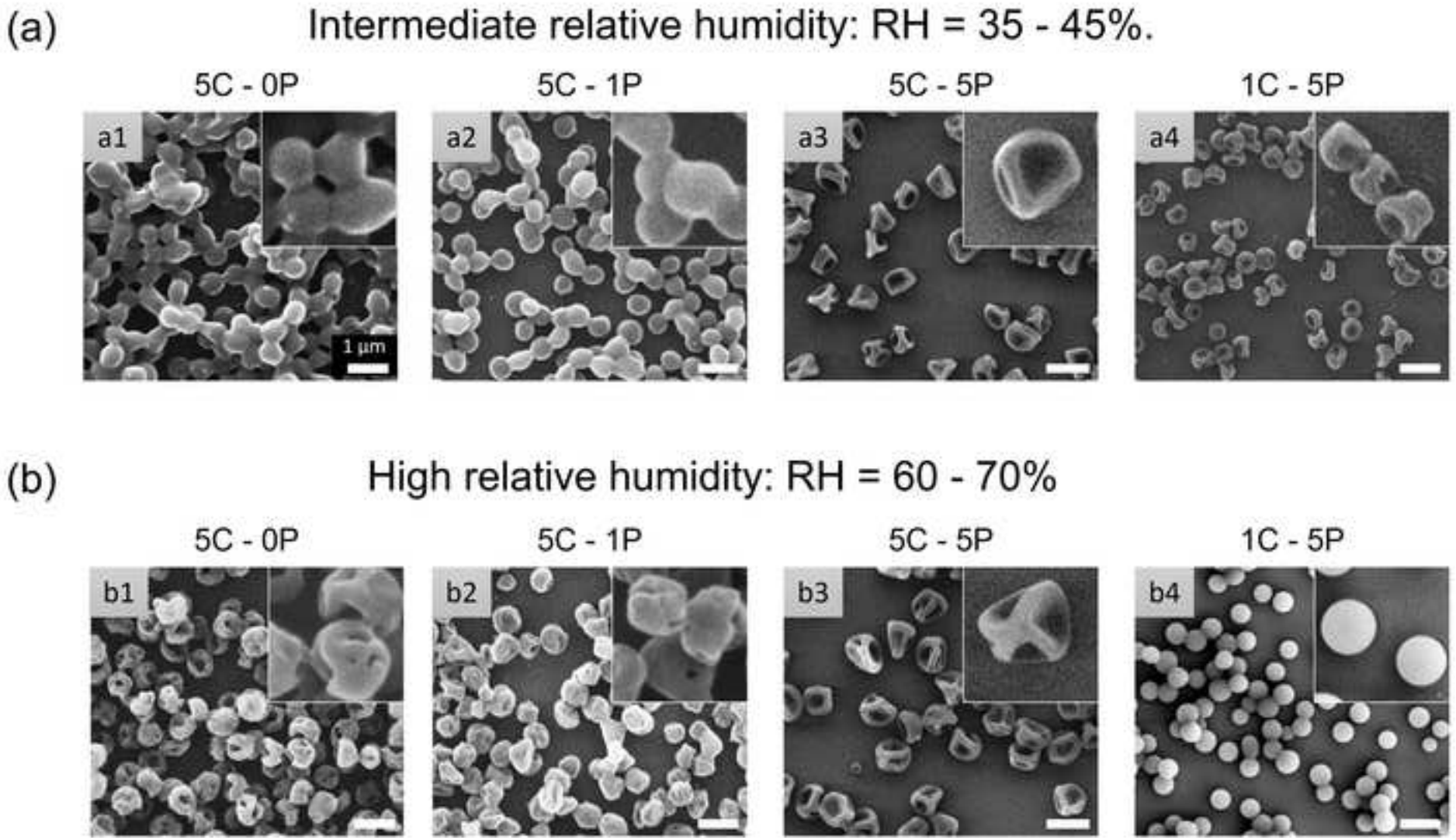
(a)
Intermediate relative humidity: RH = 35 - 45%.
5C - 0P
5C - 1P
5C - 5P
1C - 5P
a1
a2
a3
a4
1 µm
(b)
High relative humidity: RH = 60 - 70%
5C - 0P
5C - 1P
5C - 5P
1C - 5P
b1
b2
b3
b4

Figure 10

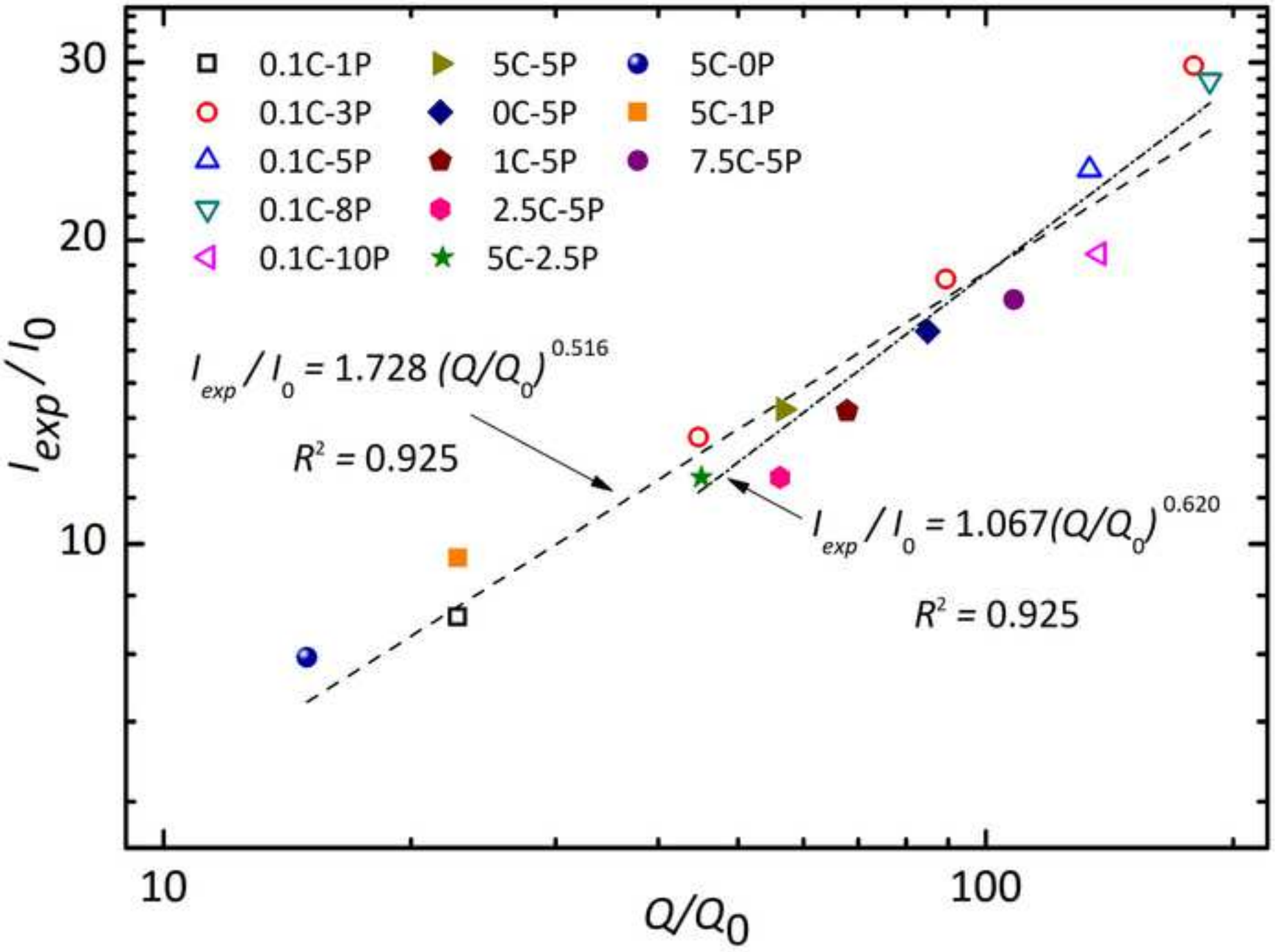
0.1C-1P
0.1C-3P
0.1C-5P
0.1C-8P
0.1C-10P
5C-5P
0C-5P
1C-5P
2.5C-5P
5C-2.5P
5C-0P
5C-1P
7.5C-5P
$I_{exp} / I_0 = 1.728\ (Q/Q_0)^{0.516}$
$R^2 = 0.925$
$I_{exp} / I_0 = 1.067(Q/Q_0)^{0.620}$
$R^2 = 0.925$
I_{exp} / I_0
Q/Q_0
30
20
10
10
100

Figure 11

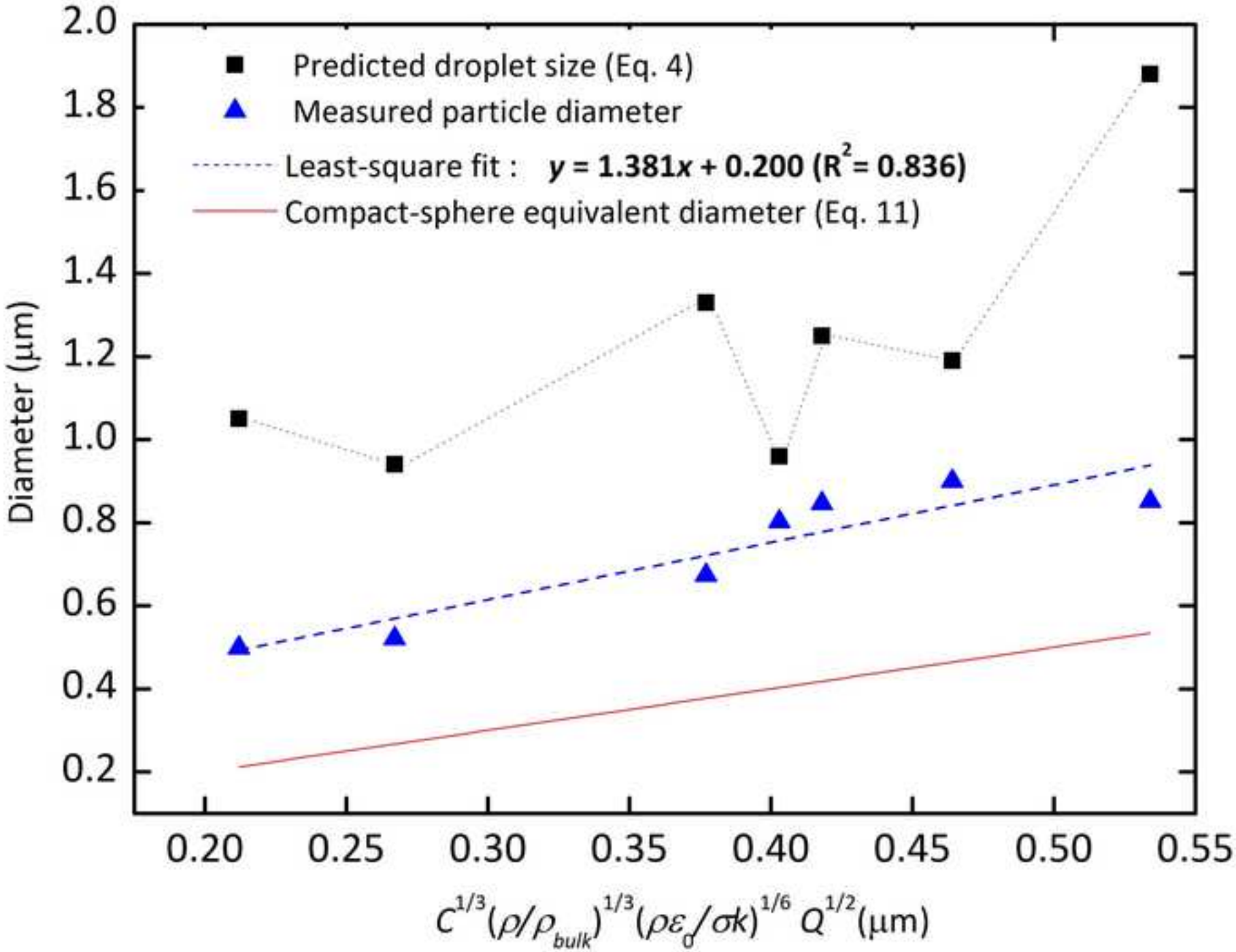
Predicted droplet size (Eq. 4)
Measured particle diameter
Least-square fit : y = 1.381x + 0.200 (R² = 0.836)
Compact-sphere equivalent diameter (Eq. 11)
Diameter (μm)
2.0
1.8
1.6
1.4
1.2
1.0
0.8
0.6
0.4
0.2
0.20
0.25
0.30
0.35
0.40
0.45
0.50
0.55
$C^{1/3}(\rho/\rho_{bulk})^{1/3}(\rho\varepsilon_0/\sigma k)^{1/6}\,Q^{1/2}$(μm)

Figure 12

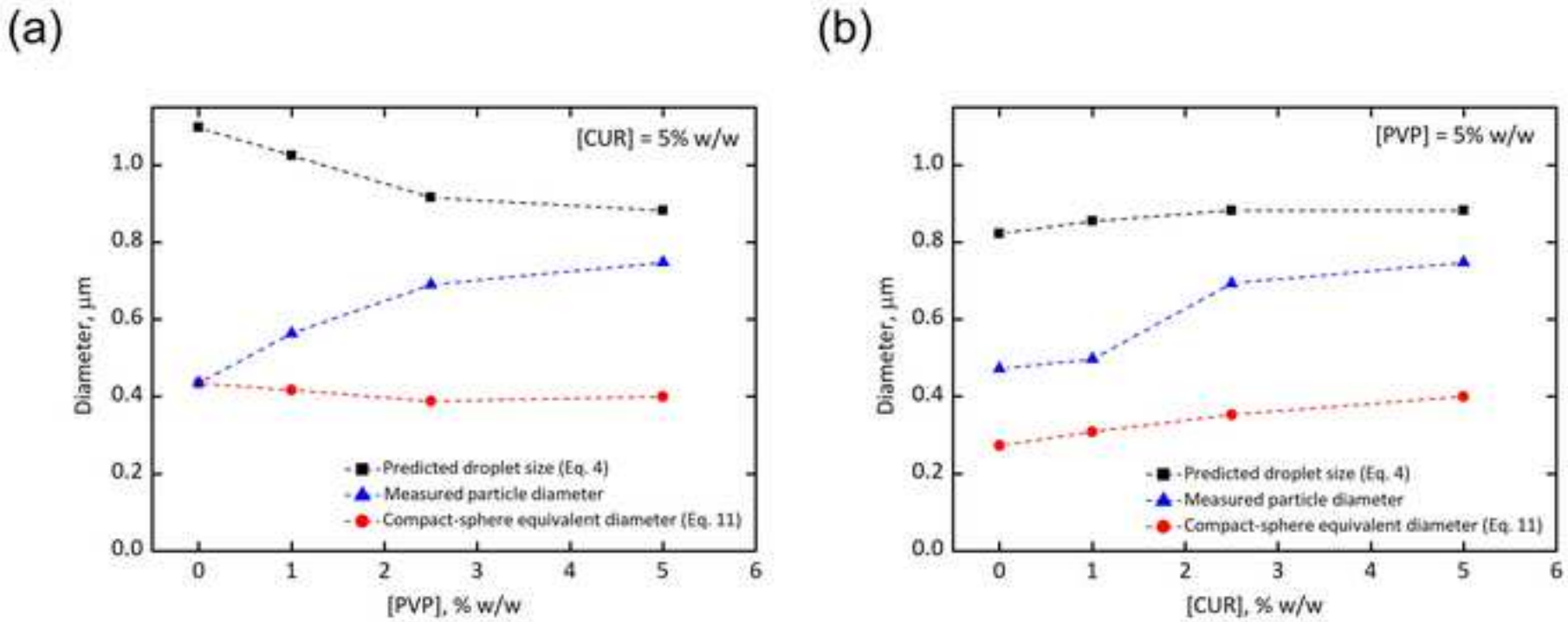
(a)
[CUR] = 5% w/w
Diameter, µm
[PVP], % w/w
Predicted droplet size (Eq. 4)
Measured particle diameter
Compact-sphere equivalent diameter (Eq. 11)
(b)
[PVP] = 5% w/w
Diameter, µm
[CUR], % w/w
Predicted droplet size (Eq. 4)
Measured particle diameter
Compact-sphere equivalent diameter (Eq. 11)

Figure 13

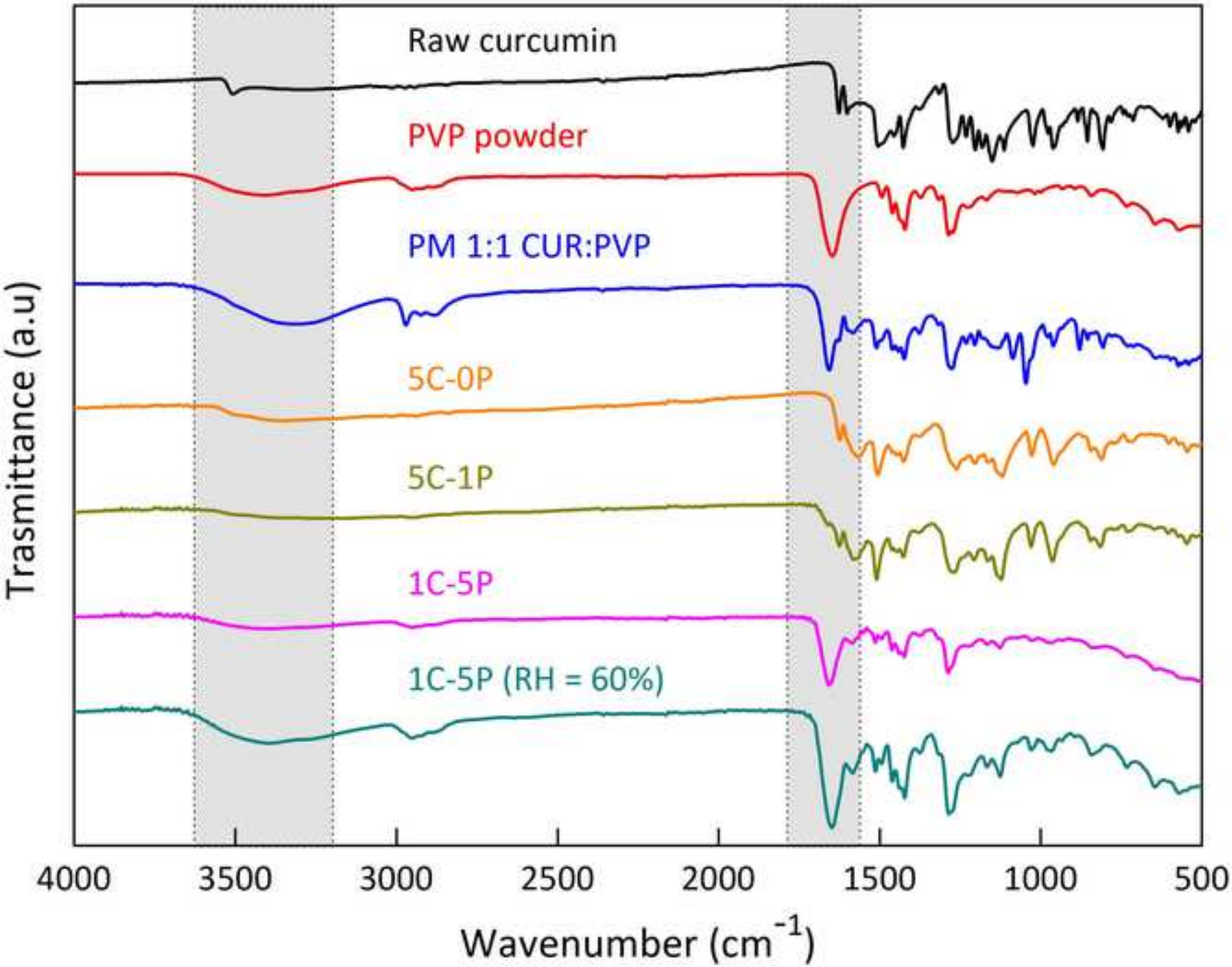
Raw curcumin
PVP powder
PM 1:1 CUR:PVP
5C-0P
5C-1P
1C-5P
1C-5P (RH = 60%)
Trasmittance (a.u)
4000
3500
3000
2500
2000
1500
1000
500
Wavenumber (cm-1)

Figure 14

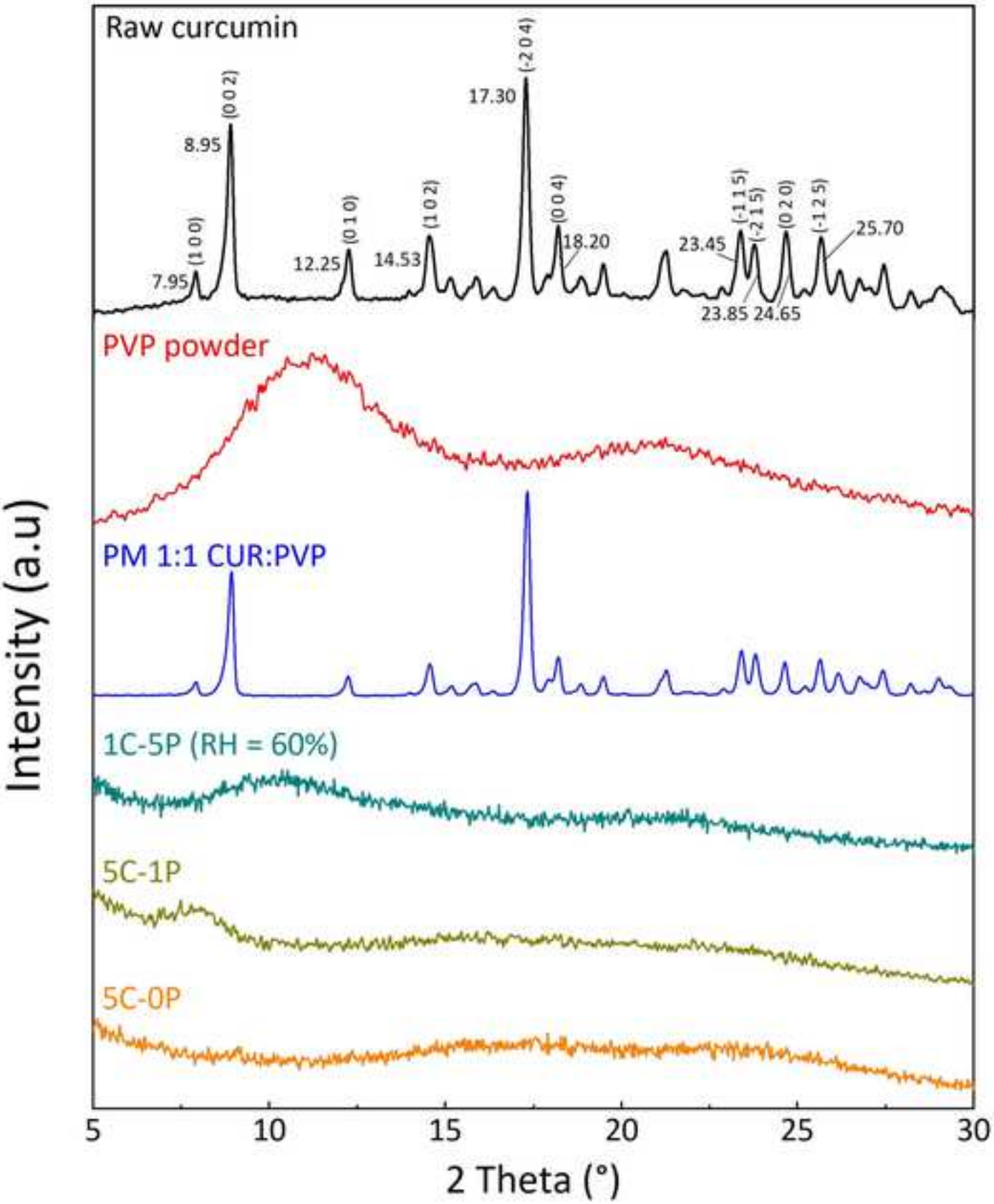
Raw curcumin
(0 0 2)
8.95
(1 0 0)
7.95
12.25
(0 1 0)
14.53
(1 0 2)
17.30
(-2 0 4)
(0 0 4)
18.20
23.45
(-1 1 5)
(-2 1 5)
(0 2 0)
23.85
24.65
(-1 2 5)
25.70
PVP powder
PM 1:1 CUR:PVP
1C-5P (RH = 60%)
5C-1P
5C-0P
Intensity (a.u)
5
10
15
20
25
30
2 Theta (°)